Isogeometric boundary element methods for three dimensional fatigue crack growth

X. Peng[1], E. Atroshchenko[2], P. Kerfriden[1], S. P. A. Bordas[3,1,4¶]

[1]Institute of Mechanics Materials and Advanced Manufacturing, Cardiff University, CF24 3AA, UK

[2]Department of Mechanical Engineering, University of Chile, Santiago, 8370448, Chile

[3]Université du Luxembourg, Faculté des Sciences, de la Technologie et de la Communication, 6, rue Richard Coudenhove-Kalergi, L-1359 Luxembourg – Research Unit in Engineering Science Campus Kirchberg, G 007

[4]Honorary Professor, Intelligent Systems for Medicine Laboratory, School of Mechanical and Chemical Engineering, The University of Western Australia (M050), 35 Stirling Highway, Crawley, WA 6009, Australia

ABSTRACT

The isogeometric boundary element method (IGABEM) based on NURBS is adopted to model fracture problem in 3D. The NURBS basis functions are used in both crack representation and physical quantity approximation. A stable quadrature scheme for singular integration is proposed to enhance the robustness of the method in dealing with highly distorted element. The convergence study in crack opening displacement is performed for penny-shaped crack and elliptical crack. Two ways to extract stress intensity factors (SIFs), the contour M integral and virtual crack closure integral, are implemented based on the framework of dual integral equations. An algorithm is outlined and validated to be stable for fatigue crack growth, thanks to the smoothness not only in crack geometry but also in stress/SIFs solution brought by IGABEM.

Key Words: *Isogeometric analysis; NURBS; Linear elastic fracture; Boundary element method; Crack growth.*

¶Corresponding author. Tel:(+352)4666445567,(+352)621131048 Fax:(+352)46664435567
E-mail address:stephane.bordas@alum.northwestern.edu

1 Introduction

The simulation of the fatigue fracture propagation is not only crucial to perform the damage tolerance assessment or predict the serving life of a mechanical component, but also to help get understand of the mechanism of structure's failure in engineering. Versatile numerical methods have been attempted for modeling fatigue fracture with the development of computational mechanics in past decades. Challenges for numerical fracture modeling primarily lie in the meshing/re-meshing procedure, as the initiation of the cracks are usually two or more orders smaller in geometry size than the components. The different scale of the cracks and components requires a local refined mesh for the nucleation of the defects and re-meshing become necessary for accurate simulation when the cracks propagate.

The finite element method (FEM) can be applied to simulate the crack propagation directly with certain adaptive re-meshing operation [1][2][3]. Some software packages have been developed based on this idea [4][5] and a review paper can be referred [6]. Nevertheless, the re-meshing becomes cumbersome for multi-cracks or for very complicated components as the complexity is increased due to the presence of cracks as internal boundaries.

The idea of partition of unity (PU) enrichment has been proposed to release the mesh burden in fracture modeling [7]. Due to the additional enrichment functions, the discontinuities are introduced into the model and the representation of the crack only aims for initiating the enrichments, which makes the crack mesh independent from the component's mesh. The extended finite element method (XFEM) [8], usually coupled with the level set functions as an implicit representation of the crack, has been implemented for 3D crack growth problem [9][10][11][12] as well as for industrial applications [13][14][15]. The meshfree methods have also been proposed with the aim of further reducing the mesh burden, for instance, the element-free Galerkin (EFG) [16] and the extended EFG (XEFG) [17][18][19]. For more details, the readers could refer the review paper by Nguyen *et al* [20].

The fracture modeling by the boundary element method (BEM) exhibits more advantages than by FEM in terms of mesh/re-mesh efforts as only the boundary discretization is required in BEM in order to approximate the quantity of interest. When cracks evolve, only the boundary surfaces are updated instead of re-generating the volume mesh. In order to circumvent the singular system caused by the collapsed surfaces in fracture, Hong and Chen [21] proposed

the dual boundary integral representations by introducing the hyper-singular equation derived from the secondary field [22]. The use of dual boundary integral equation makes the crack propagation simulation more effective through a single domain. And the corresponding dual BEM was subsequently implemented for 2D and 3D fracture [23][24][25] and was extended to material-nonlinear fracture [26][27] and dynamic crack propagation [28]. Commercial packages based on BEM are BEASY [29] and FRANC3D [30]. Apart from the dual BEM based on the collocation method, the Galerkin BEM, in particular the symmetric Galerkin BEM (SGBEM) has also drawn attention in the application for fracture analysis [31][32][33]. The symmetric matrix system of SGBEM also facilitates the coupling with FEM [34][35].

The isogeometric analysis (IGA) was first introduced by Hughes *et al* [36]. The basic idea of IGA is to use the same spline basis functions to represent the CAD geometries and approximate the physical quantities of interest. And the investigation on the joint of IGA and BEM (IGABEM) has increasingly drawn attention recently since only the boundary representation of the geometry is required in IGABEM, which facilitates the integration of design and analysis. The IGABEM has already been applied in many fields [37][38][39][40][41][42][43][44], and has been further developed with more numerical aspects such as the PU enrichment [45][46], the trimmed NURBS [47][48], the fast solution [49], the Galerkin form [50][51] etc. The benefit of smoothness to boundary integrals (BIEs) brought by IGA is investigated in [52].

The isogeometric analysis has been applied to fracture in corporation with XFEM [53][54][55][56]. Verhoosel *et al* presented a scheme to model cohesive crack propagation by using T-splines to generate the local discontinuities [57]. Nguyen *et al* applied the B-spline based IGA to simulate the 2D and 3D delamination in composites [58]. The shape sensitivity analysis of stress intensity factors for curved cracks was performed by Choi and Cho [59]. Tambat *et al* proposed an enriched IGAFEM based on the CAD-inspired hierachical partition of unity field compositions, and the method benefits from a robust and non-iterative numerical distance field construction [60][61]. Jeong *et al* proposed a geometrical mapping by which push-forwards of B-splines from the parameter space into the physical space such that the singularity of type $r^{1/2}$ can be captured in linear elastic cracks [62][63]. Natarajan *et al* enhanced the isogeometric analysis by the scaled boundary finite element method which inherits both advantages of FEM and IGABEM, while certain subdivision of the domain needs to be done for complicated geometry in order to obtain the scaling center [64]. The pivot tips of the application in fracture in the IGA

framework can be concluded as:

(1) The higher-order continuity improves the accuracy of the stress field near the crack tip which is crucial to fracture analysis and the degrees of freedom is reduced compared to the C^0 Lagrange basis;
(2) The curvature, tangential and normal vectors are exactly retained and evolved thanks to the exact representation of the curved cracks;
(3) The local crack tip (front) system can be constructed directly based on the spline-based curve or surface-represented cracks, which helps to accurately evaluate the fracture parameters;
(4) The concept of integration through design to analysis facilities the mechanical/structural design based on the fatigue fracture analysis.

In this work, the application of IGABEM in 3D fracture analysis and fatigue crack growth will be explored. Besides using the conventional boundary integral equation as for elasticity, the hyper-singular integral equation is introduced additionally by exploiting the smoothness of NURBS geometries. An local singularity removing technique proposed by Guiggiani [65] is applied on the various orders of singular integrals (up to hyper-singular $O(1/r^3)$), and its improved version tailored to distorted elements (or with high aspect ratio) which commonly arise in isogeometric based methods is formulated. The crack is explicitly represented by NURBS surface as internal boundary and an algorithm is outlined to describe the crack propagation such that the smoothness in geometry brought by IGA and in solution brought by BEM is fully investigated for extracting the stress intensity factors and crack growth.

The rest of the paper is organized as follows. Section 2 briefs the boundary integral equations (BIEs) that applied in fracture modeling. Section 3 illustrates the NURBS basis functions on 2D surfaces and the collocation scheme. Section 4 outlines the improved singular integration based on the singularity subtraction technique [65]. The crack growth related work is detailed in section 5, including updating the crack surface geometrically, computing the stress intensity factors and the fatigue fracture rule: the Paris law. Numerical examples for both static fracture analysis and crack growth are given in section 6. We conclude our work and propose the future research of interest in the last section.

2 Boundary integral equations for crack modeling

Consider an arbitrary domain Ω which contains a crack as in Figure 1. The boundary of the domain $\partial\Omega = S + S_{c^+} + S_{c^-}$, where S is composed of S_u where Dirichlet boundary conditions are prescribed (known displacement $\bar{\mathbf{u}}$), S_t where Neumann boundary conditions are prescribed (known traction $\bar{\mathbf{t}}$). The displacement BIE is given by finding $\mathbf{u}$ and $\mathbf{t}$ such that

$$c_{ij}(\mathbf{s})u_j(\mathbf{s}) = \int_{\partial\Omega} U_{ij}(\mathbf{s},\mathbf{x})t_j(\mathbf{x})\mathrm{d}S(\mathbf{x}) - \fint_{\partial\Omega} T_{ij}(\mathbf{s},\mathbf{x})u_j(\mathbf{x})\mathrm{d}S(\mathbf{x}), \tag{1}$$

where the U_{ij}, T_{ij} are called fundamental solutions and for linear elasticity,

$$U_{ij}(\mathbf{s},\mathbf{x}) = \frac{1}{16\pi\mu(1-\nu)r}\left[(3-4\nu)\delta_{ij} + r_{,i}r_{,j}\right], \tag{2}$$

$$T_{ij}(\mathbf{s},\mathbf{x}) = -\frac{1}{8\pi(1-\nu)r^2}\left\{\frac{\partial r}{\partial n}[(1-2\nu)\delta_{ij} + 3r_{,i}r_{,j}] - (1-2\nu)(r_{,i}n_j - r_{,j}n_i)\right\}, \tag{3}$$

where $\mu = E/[2(1+\nu)]$, E is Young's Modulus and ν Poisson's ratio. $\mathbf{s}$ is the source point (or collocation point. This two terms will be used interchangeably in the remainder part of this paper). $\fint$ denotes the integral is interpreted in the *Cauchy Principal Value* sense. The traction BIE is obtained by differentiation of the displacement BIE with respect to $\mathbf{s}$ and multiplication by the elastic tensor E_{ijkl}:

$$c_{ij}(\mathbf{s})t_j(\mathbf{s}) = \fint_{\partial\Omega} K_{ij}(\mathbf{s},\mathbf{x})t_j(\mathbf{x})\mathrm{d}S(\mathbf{x}) - \fint\!\!\!\fint_{\partial\Omega} H_{ij}(\mathbf{s},\mathbf{x})u_j(\mathbf{x})\mathrm{d}S(\mathbf{x}), \tag{4}$$

$$H_{ij}(\mathbf{s},\mathbf{x}) = E_{ikpq}\frac{\partial T_{pj}(\mathbf{s},\mathbf{x})}{\partial s_q}n_k(\mathbf{s}), \quad K_{ij}(\mathbf{s},\mathbf{x}) = E_{ikpq}\frac{\partial U_{pj}(\mathbf{s},\mathbf{x})}{\partial s_q}n_k(\mathbf{s}), \tag{5}$$

where $\fint\!\!\!\fint$ denotes the *Hadamard Finite Part* integral.

The idea of the boundary element method is to discretize the boundary geometry and the physical fields using sets of basis functions. Subsequently, the source point is placed at the collocation points and the displacement BIE (1) is transformed into the system of linear algebraic equations. However, when the domain contains a crack, the collocation points on the overlapping surfaces S_{c^+} and S_{c^-} could be coincided (refer to Figure 1 (b)), and then the system matrix becomes singular. Two ways to deal with this problem are briefed in the following sections.

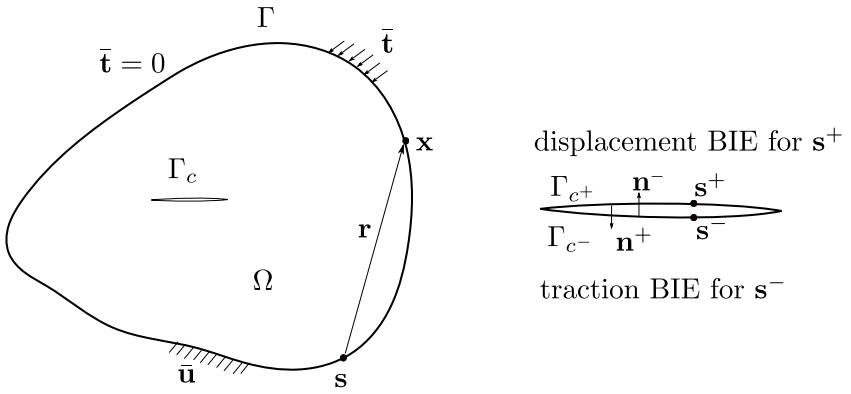

(a) (b)

Figure 1: Crack model

2.1 Dual equations

The difficulty caused by the collapsed crack surfaces is circumvented through the use of dual equations, by prescribing the displacement BIE (Equation (1)) on one crack surface (S_{c^+}) and on the rest of the boundary S. For the collocation point $\mathbf{s}^+$ on the crack surface S_{c^+}, Equation (1) can be rewritten as,

$$\begin{aligned} c_{ij}(\mathbf{s}^+)u_j(\mathbf{s}^+) + c_{ij}(\mathbf{s}_m^-)u_j(\mathbf{s}^+) = &\int_S U_{ij}(\mathbf{s}^+,\mathbf{x})t_j(\mathbf{x})\mathrm{d}S(\mathbf{x}) - \int_S T_{ij}(\mathbf{s}^+,\mathbf{x})u_j(\mathbf{x})\mathrm{d}S(\mathbf{x}) \\ &- \cancel{\int}_{S_{c^+}} T_{ij}(\mathbf{s}^+,\mathbf{x}^+)u_j(\mathbf{x}^+)\mathrm{d}S(\mathbf{x}) - \cancel{\int}_{S_{c^-}} T_{ij}(\mathbf{s}_m^-,\mathbf{x}^-)u_j(\mathbf{x}^-)\mathrm{d}S(\mathbf{x}) \\ &+ \int_{S_{c^+}} U_{ij}(\mathbf{s}^+,\mathbf{x}^+)t_j(\mathbf{x}^+)\mathrm{d}S(\mathbf{x}) + \int_{S_{c^-}} U_{ij}(\mathbf{s}_m^-,\mathbf{x}^-)t_j(\mathbf{x}^-)\mathrm{d}S(\mathbf{x}). \end{aligned} \tag{6}$$

And analogously, the traction BIE (Equation (4)) on the other crack surface (S_{c^-} in Figure 1(b)) becomes,

$$\begin{aligned} c_{ij}(\mathbf{s}^-)t_j(\mathbf{s}^-) + c_{ij}(\mathbf{s}_m^+)t_j(\mathbf{s}^-) = &\int_S K_{ij}(\mathbf{s}^-,\mathbf{x})t_j(\mathbf{x})\mathrm{d}S(\mathbf{x}) - \int_S H_{ij}(\mathbf{s}^-,\mathbf{x})u_j(\mathbf{x})\mathrm{d}S(\mathbf{x}) \\ &- \cancel{\int}_{S_{c^-}} H_{ij}(\mathbf{s}^-,\mathbf{x}^-)u_j(\mathbf{x}^-)\mathrm{d}S(\mathbf{x}) + \cancel{\int}_{S_{c^+}} H_{ij}(\mathbf{s}_m^+,\mathbf{x}^+)u_j(\mathbf{x}^+)\mathrm{d}S(\mathbf{x}) \\ &+ \cancel{\int}_{S_{c^-}} K_{ij}(\mathbf{s}^-,\mathbf{x}^-)t_j(\mathbf{x}^-)\mathrm{d}S(\mathbf{x}) - \cancel{\int}_{S_{c^+}} K_{ij}(\mathbf{s}_m^+,\mathbf{x}^-)t_j(\mathbf{x}^+)\mathrm{d}S(\mathbf{x}). \end{aligned} \tag{7}$$

$\mathbf{s}_m^-$ denotes the mirror point of $\mathbf{s}^+$ on the S_{c^-}, which means $\mathbf{s}_m^-$ and $\mathbf{s}^-$ share the same physical and parametric coordinate but the normal vectors at each are opposite. The last two terms of both equations and left hand side of Equation (7) are omitted due to the fraction-free crack.

Due to the collapse boundary in fracture problem, two jump terms arise in each BIE and each operator not only exhibits singularity on the crack surface where the collocation points located, but also on the one where the mirror points of the collocation points located.

2.2 Crack opening displacement (COD) equation

The boundary integral equation for crack problem can also be reformulated by setting the boundary quantity as crack opening displacement over a couple of crack surfaces. Let the source point approach to a single crack surface, for example $S_c = S_{c^+}$, and note that $\mathbf{n} = \mathbf{n}^+ = -\mathbf{n}^-$, we have:

$$\begin{aligned} c_{ij}(\mathbf{s}^+)u_j(\mathbf{s}^+) + c_{ij}(\mathbf{s}^-)u_j(\mathbf{s}^-) = &\int_S U_{ij}(\mathbf{s}^+,\mathbf{x})t_j(\mathbf{x})\mathrm{d}S(\mathbf{x}) - \fint_S T_{ij}(\mathbf{s}^+,\mathbf{x})u_j(\mathbf{x})\mathrm{d}S(\mathbf{x}) \\ &+ \int_{S_c} U_{ij}(\mathbf{s}^+,\mathbf{x}^+)(t_j(\mathbf{x}^+) + t_j(\mathbf{x}^-))\mathrm{d}S(\mathbf{x}) \\ &- \fint_{S_c} T_{ij}(\mathbf{s}^+,\mathbf{x}^+)(u_j(\mathbf{x}^+) - u_j(\mathbf{x}^-))\mathrm{d}S(\mathbf{x}). \end{aligned} \tag{8}$$

The corresponding traction BIE is:

$$\begin{aligned} c_{ij}(\mathbf{s}^+)t_j(\mathbf{s}^+) - c_{ij}(\mathbf{s}^-)t_j(\mathbf{s}^-) = &\fint_S K_{ij}(\mathbf{s}^+,\mathbf{x})t_j(\mathbf{x})\mathrm{d}S(\mathbf{x}) - \fint_S H_{ij}(\mathbf{s}^+,\mathbf{x})u_j(\mathbf{x})\mathrm{d}S(\mathbf{x}) \\ &+ \fint_{S_c} K_{ij}(\mathbf{s}^+,\mathbf{x}^+)(t_j(\mathbf{x}^+) + t_j(\mathbf{x}^-))\mathrm{d}S(\mathbf{x}) \\ &- \fint_{S_c} H_{ij}(\mathbf{s}^+,\mathbf{x}^+)(u_j(\mathbf{x}^+) - u_j(\mathbf{x}^-))\mathrm{d}S(\mathbf{x}). \end{aligned} \tag{9}$$

Equation (9) can be used alone if only the COD will be presented as the unknown for fatigue fracture problem. However if the displacement field needs to be known on the crack surfaces, Equation (8) should be also solved. Let $S \to \infty$, and note that traction-free crack surfaces are assumed, we arrive at:

$$0 = t_j^\infty(\mathbf{s}) - \fint_{S_c} H_{ij}(\mathbf{s},\mathbf{x})[\![u_j(\mathbf{x})]\!]\mathrm{d}S(\mathbf{x}). \tag{10}$$

$[\![u_j(\mathbf{x})]\!] = u_j(\mathbf{x}^+) - u_j(\mathbf{x}^-)$ is the crack opening displacement. All the subscripts '+' are omitted since the integral is only over a single crack surface. $\mathbf{t}^\infty$ is interpreted as the solution in the 'no crack' space.

3 NURBS discretization and collocation

NURBS basis functions are the generalization of B-spline functions that allows a 'projection' from square and cubic domains to form complex geometries. So the basic concept of B-spline is first outlined. B-spline basis functions are defined over a knot vector, which is a non-decreasing sequence of real numbers given in the parameter space. A knot vector is denoted as $\Xi = \{\xi_1, \xi_2, ..., \xi_{n+p+1}\}$, where $\xi_i \in \mathbb{R}$ is the i^{th} parameter coordinate (knot), p is the order of the polynomial in B-spline basis functions, n is the number of the basis functions. For a given order p, the B-spline basis functions $N_{i,p}$ with $1 \leqslant a \leqslant n$ are defined by the Cox-de Boor recursion:

$$N_{i,0}(\xi) = \begin{cases} 1 & \xi_i \leqslant \xi < \xi_{i+1} \\ 0 & \text{otherwise,} \end{cases} \tag{11}$$

then, for $p > 0$,

$$N_{i,p}(\xi) = \frac{\xi - \xi_i}{\xi_{i+p} - \xi_i} N_{i,p-1}(\xi) + \frac{\xi_{i+p+1} - \xi}{\xi_{i+p+1} - \xi_{i+1}} N_{i+1,p-1}(\xi). \tag{12}$$

The continuity of B-spline basis functions at ξ_i can be decreased by repeating the knot several times. If ξ_i has multiplicity k ($\xi_i = \xi_{i+1} = ... = \xi_{i+k-1}$), then the basis functions are C^{p-k} continuous at ξ_i. Particularly, when $k = p$, the basis is C^0 and $k = p+1$ leads to a discontinuity at ξ_i. If the first and last knot have $k = p + 1$, the knot vector is called an open knot vector. More details can be referred in [66].

Given the knot vectors $\Xi = \{\xi_1, \xi_2, ..., \xi_{n+p+1}\}$ and $\mathscr{H} = \{\eta_1, \eta_2, ..., \eta_{m+q+1}\}$, and the control points net $P_{i,j}$. The B-spline surface $S(\xi, \eta)$ is given by the tensor-product of B-spline basis functions defined in 2D parametric domain $[\xi_1, \xi_{n+p+1}] \times [\eta_1, \eta_{m+q+1}]$,

$$S(\xi, \eta) = \sum_{i=1}^{n} \sum_{j=1}^{m} N_{i,p}(\xi) M_{j,q}(\eta) P_{i,j}, \tag{13}$$

where $N_{i,p}(\xi)M_{j,q}(\eta)$ are the 2D B-spline basis functions. The NURBS basis functions can be constructed by rationalizing the tensor-product B-spline basis functions as

$$R_{i,j}(\xi, \eta) = \frac{N_{i,p}(\xi) M_{j,q}(\eta) w_{i,j}}{\sum_{k=1}^{n} \sum_{l=1}^{m} N_{k,p}(\xi) M_{l,q}(\eta) w_{k,l}}, \tag{14}$$

where the scalar variable $w_{i,j}$ is the weight associated with the control point $P_{i,j}$. For integration purpose, the 2D NURBS basis functions are usually calculated in the element defined by the non-zero knot intervals $[\xi_i, \xi_{i+1}] \times [\eta_j, \eta_{j+1}]$ where the Gaussian rule can be applied [36].

The Greville abscissae has been used to generate the collocation points. For a closed domain composed by trimless and compatible NURBS patches, the number of obtained collocation points by the Greville abscissae is identical to the number of control points (or basis functions), which means one collocation point is associated with one control point. For those collocation points lie in the sharp edges or corners, or when discontinuous basis functions are needed, these collocation points will be offset from the original place by

$$\begin{aligned} \xi_{s,i} &= \xi_{s,i} + \alpha(\xi_{s,i+1} - \xi_{s,i}), \quad \text{or} \\ \xi_{s,i} &= \xi_{s,i} - \alpha(\xi_{s,i} - \xi_{s,i-1}), \quad \alpha \in (0,1). \end{aligned} \tag{15}$$

Note that in this case, the associated control points should be doubled such that the discontinuous basis functions are obtained, or the BIEs on the offset collocation points should be merged into one BIE, such that the number of equations and unknowns keeps consistence.

4 Numerical integration

Due to the singularities in BIEs, there will be singular integration and non-singular integration after discretization. For the element containing the collocation point, singular integration is performed and the element belongs to singular elements. Elements which exclude the collocation point are called non-singular elements. The singular integration needs to be carefully treated in BEM. Various numerical methods have been proposed in past decades, and one can refer to a review work in [22]. A robust technique developed in [67] can be applied to regularized all the singular terms into weakly singular, via the use of simple solution of BIE. The regularization technique based on simple solutions has been applied or further developed in the framework of IGABEM [39][68][52]. However, this method fails when dealing with open surfaces such as cracks [69]. In the present work, we use the singularity subtraction technique (SST) proposed by Guiggiani [69][65] to remove the singularities arise in both BIEs. The SST is a united method for the treatment of singular integrals regardless of mesh dicretization and proved to be efficient for fracture via dual BEM [24].

4.1 Singularity subtraction technique (SST) for singular integrals

The SST transforms various orders of singular integration into a weakly singular one based on the intrinsic coordinate system of the singular element after discretization. Then the weakly singular integration turns to be regular if the quadrature is performed in the polar coordinates. By expanding the integrand into a series with respect to the intrinsic coordinate, the singularity can be represented explicitly. Then the singular terms are subtracted from the integrand, leaving the remaining to be regular for which regular Gaussian rule is applied. the subtracted terms are added back semi-analytically. Assume that the coordinate of point of interest is $\mathbf{x}(x_i = x, y, z)$ in physical space, $\boldsymbol{\xi}(\xi_i = \xi, \eta)$ in parametric space of NURBS basis functions, $\bar{\boldsymbol{\xi}}(\bar{\xi}_i = \bar{\xi}, \bar{\eta})$ in parent space $[-1, 1] \times [-1, 1]$. For the hyper-singular integral of the form

$$I = \neq\!\!\!\!\int_S H(\mathbf{s}, \mathbf{x}(\bar{\boldsymbol{\xi}}))R(\bar{\boldsymbol{\xi}})\bar{J}(\bar{\boldsymbol{\xi}})\mathrm{d}S, \tag{16}$$

where $H(\mathbf{s}, \mathbf{x}(\bar{\boldsymbol{\xi}}))$ is the hyper-singular kernel, $R(\bar{\boldsymbol{\xi}})$ is the NURBS basis function and $\bar{J}(\bar{\boldsymbol{\xi}})$ is the Jacobi transformation from parent space to physical space (Figure 2). The polar coordinates $\boldsymbol{\rho}(\rho, \theta)$ centred at the source point are introduced in the parent space. The parent domain is subdivided into triangles for quadrature naturally. For each field point $\bar{\boldsymbol{\xi}}$ in the sub-triangles, we have

$$\begin{aligned} \bar{\xi} &= \bar{\xi}_s + \rho\cos\theta, \\ \bar{\eta} &= \bar{\eta}_s + \rho\sin\theta, \end{aligned} \tag{17}$$

After the polar coordinate transformation, Equation (16) becomes

$$I = \lim_{\varepsilon \to 0} \int_0^{2\pi} \int_{\alpha(\varepsilon,\theta)}^{\hat{\rho}(\theta)} H(\rho, \theta)R(\rho, \theta)\bar{J}(\rho, \theta)\rho\mathrm{d}\rho\mathrm{d}\theta, \tag{18}$$

where $\hat{\rho}(\theta) = h/\cos\bar{\theta}$. h is the shortest distance from the source point to the element edge and $\bar{\theta}$ is the angle from perpendicular direction to the field point as in Figure 2. If we define θ_0 is the angle of the perpendicular line, then the angle to the field point can be computed as

$$\theta = \bar{\theta} + \theta_0. \tag{19}$$

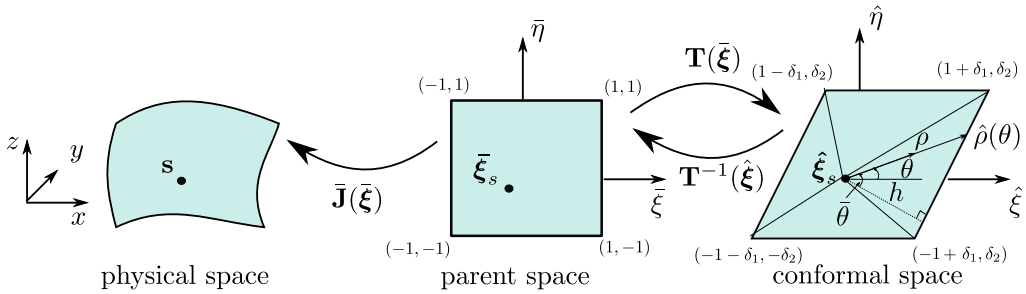

Figure 2: Transformation between coordinate system for SST

The integrand $F(\rho,\theta) = H(\rho,\theta)R(\rho,\theta)\bar{J}(\rho,\theta)\rho$ is expanded as:

$$F(\rho,\theta) = \frac{F_{-2}(\theta)}{\rho^2} + \frac{F_{-1}(\theta)}{\rho} + F_0(\theta) + F_1(\theta)\rho + F_2(\theta)\rho^2 + \cdots = \sum_{i=-1}^{\infty} F_i(\theta)\rho^i. \tag{20}$$

The first two singular terms on the right hand side are subtracted and added back semi-analytically, resulting in:

$$\begin{aligned} I &= I_1 + I_2, \\ I_1 &= \int_0^{2\pi}\int_0^{\hat{\rho}(\theta)} \Big[F(\rho,\theta) - \frac{F_{-2}(\theta)}{\rho^2} - \frac{F_{-1}(\theta)}{\rho}\Big]\mathrm{d}\rho\mathrm{d}\theta, \\ I_2 &= \int_0^{2\pi} I_{-1}(\theta)\ln\frac{\hat{\rho}(\theta)}{\beta(\theta)}\mathrm{d}\theta - \int_0^{2\pi} I_{-2}(\theta)\Big[\frac{\gamma(\theta)}{\beta^2(\theta)} + \frac{1}{\hat{\rho}(\theta)}\Big]\mathrm{d}\theta, \end{aligned} \tag{21}$$

where I_1 is regular and I_2 are regular line integrals, Both can be applied with Gaussian quadrature rule. The evaluation of $\alpha(\varepsilon,\theta)$, $\beta(\theta)$ and $\gamma(\theta)$ as well as the limiting process are given in Appendix A and more details can be referred in [65].

4.2 Conformal mapping for SST

It has been revealed by Rong *et al* [70] that the expansion coefficients $F_i(\theta)$ in Equation (20) exhibits various orders of near-singularity in the angular θ direction, although the singularity in the radial ρ direction has been fully canceled. This near-singularity is sensitive to the shape of the element and becomes severe when the element is highly distorted. The $F_i(\theta)$ can be represented as:

$$F_i(\theta) = \frac{\tilde{F}_i(\theta)}{A^p(\theta)} = \frac{\tilde{F}_i(\theta)}{[0.5(|\mathbf{m}_1^s|^2 + |\mathbf{m}_2^s|^2)(\omega\sin(2\theta+\varphi)+1)]^{p/2}}, \tag{22}$$

where $\tilde{F}_i(\theta)$ are the regular trigonometric functions and integer 'p' is the order associated with 'i'. The curve-linear basis vectors $\mathbf{m}_i^s = \mathbf{m}_i|_{\bar{\boldsymbol{\xi}}=\bar{\boldsymbol{\xi}}_s}, (i = 1, 2)$ and are calculated as:

$$\begin{aligned} \mathbf{m}_1 &= \Big[\frac{\partial x}{\partial \bar{\xi}}, \frac{\partial y}{\partial \bar{\xi}}, \frac{\partial z}{\partial \bar{\xi}}\Big], \\ \mathbf{m}_2 &= \Big[\frac{\partial x}{\partial \bar{\eta}}, \frac{\partial y}{\partial \bar{\eta}}, \frac{\partial z}{\partial \bar{\eta}}\Big]. \end{aligned} \tag{23}$$

Introducing two parameters

$$\begin{aligned} \lambda &= |\mathbf{m}_1^s|/|\mathbf{m}_2^s|, \\ \cos\psi &= \mathbf{m}_1^s \cdot \mathbf{m}_2^s/|\mathbf{m}_1^s||\mathbf{m}_2^s|, \end{aligned} \tag{24}$$

such that

$$\begin{aligned} \varphi &= \arctan\frac{\lambda^2 - 1}{2\lambda\cos\psi}, \\ \omega &= \sqrt{1 - \frac{4\sin^2\psi}{(\lambda + \lambda^{-1})^2}} < 1. \end{aligned} \tag{25}$$

Then it can be concluded that when the element aspect ratio is large or angle between two basis vectors tends to 0 or π ($\sin\psi \to 0$), $A(\theta)$ will tend to 0, resulting the near-singularity of $F_i(\theta)$. Both scenarios indicate a distorted shape of the singular element, which are common phenomenon in isogeometric analysis.

Rong *et al* [70] constructed the conformal mapping from the parent space $(\bar{\xi}, \bar{\eta})$ to a new parametric space $(\hat{\xi}, \hat{\eta})$ where the two curve linear basis vectors in the new parametric space are orthogonal and have identical length to each other, i.e.

$$\begin{aligned} \hat{\mathbf{m}}_1^s \cdot \hat{\mathbf{m}}_2^s &= 0, \\ |\hat{\mathbf{m}}_1^s| &= |\hat{\mathbf{m}}_2^s|. \end{aligned} \tag{26}$$

Then $A(\theta)$ becomes a constant, which makes the integration nonsensitive to the element shape, if the series is expanded in the new space. The quadrature for the singular integral turns to be stable regardless the distorted mesh.

The mapping proposed by Rong *et al* is tailored for triangular element, in this work we extend it into the quadrilateral element (Figure (2)). In [70], the Jacobian transformation matrix $\mathbf{T}$

from $(\bar{\xi}, \bar{\eta})$ to a new parametric space $(\hat{\xi}, \hat{\eta})$ is

$$\mathbf{T} = \begin{bmatrix} 1 & \delta_1 \\ 0 & \delta_2 \end{bmatrix}, \text{ so that } \hat{\boldsymbol{\xi}} = \mathbf{T}\bar{\boldsymbol{\xi}}, \tag{27}$$

where $\delta_1 = \cos\psi/\lambda$, $\delta_2 = \sin\psi/\lambda$. Then the new basis vectors

$$\begin{bmatrix} \hat{\mathbf{m}}_1^s & \hat{\mathbf{m}}_2^s \end{bmatrix} = \begin{bmatrix} \mathbf{m}_1^s & \mathbf{m}_2^s \end{bmatrix} \mathbf{T}^{-1} = \begin{bmatrix} \mathbf{m}_1^s & -(\delta_1/\delta_2)\mathbf{m}_1^s + (1/\delta_2)\mathbf{m}_2^s \end{bmatrix} \tag{28}$$

will satisfy the relation in Equations (26). The bilinear interpolation is used from $(\bar{\xi}, \bar{\eta})$ to the new parametric space $(\hat{\xi}, \hat{\eta})$ for a quadrilateral element:

$$\begin{aligned} \hat{\boldsymbol{\xi}} &= \sum_{I=1}^{4} N_I(\bar{\boldsymbol{\xi}})\hat{\boldsymbol{\xi}}^I, \\ N_1 &= 0.25(\bar{\xi} - 1)(\bar{\eta} - 1), \\ N_2 &= 0.25(\bar{\xi} + 1)(\bar{\eta} - 1), \\ N_3 &= 0.25(\bar{\xi} + 1)(\bar{\eta} + 1), \\ N_4 &= 0.25(\bar{\xi} - 1)(\bar{\eta} + 1). \end{aligned} \tag{29}$$

Combining Equations (27) and (29), the nodal coordinates $\hat{\boldsymbol{\xi}}^I$ can be obtained as $\hat{\boldsymbol{\xi}}^1(1+\delta_1, \delta_2)$, $\hat{\boldsymbol{\xi}}^2(-1+\delta_1, \delta_2)$, $\hat{\boldsymbol{\xi}}^3(-1-\delta_1, -\delta_2)$ and $\hat{\boldsymbol{\xi}}^4(1-\delta_1, -\delta_2)$. It should be noted that since $0 < \psi < \pi$, $\delta_2 > 0$, the quadrilateral element is guaranteed to have positive area (one possible plot is shown in Figure (2)). This requires the source point should not be located in the degenerated point in the geometry where $|\mathbf{m}_i^s| \neq 0$.

It can be referred from Figure 2 that the shape of the element in conformal space is controlled by the coefficients δ_1 and δ_2. This means that if λ (reflect element aspect ratio) and $\cos\psi$ (reflect element distortion) deviate from 1, the conformal element will be skew. This will result in sub-triangles with $\bar{\theta}$ approaches to $\pm\pi/2$ if the field point closed to the edges adjacent to the source point of the sub-triangles (Figure 2). Thus $\hat{\rho}(\theta) = h/\cos\bar{\theta}$ is not calculated accurately. To alleviate this near singularity in $\hat{\rho}(\theta)$, the following Sigmoidal transformation is applied in the angular direction such that the integration points will be clustered to the edges where the near-singularity is severe adaptively according to the $\bar{\theta}$ [70],

$$
\begin{aligned}
w(\bar{\theta}) &= \frac{1}{\pi}\Big(\bar{\theta}+\frac{\pi}{2}\Big), \quad \bar{\theta}\in(-\frac{\pi}{2},\frac{\pi}{2}), z\in(0,1)\\
z &= z(s) = w(\bar{\theta}_1)+\frac{1}{2}(s+1)(w(\bar{\theta}_2)-w(\bar{\theta}_1)), \quad s\in(-1,1), z\in(z(\bar{\theta}_1),z(\bar{\theta}_2))\subset(0,1)\\
f(z) &= \frac{z^m}{z^m+(1-z)^m},\\
\bar{\theta} &= \pi f(z)-\frac{\pi}{2},\\
J^{-1}(\theta) &= \frac{\partial\theta}{\partial s} = \frac{\pi[w(\bar{\theta}_2)-w(\bar{\theta}_1)]mf(z)^{m-1}}{2(f(z)^m+(1-f(z))^m)^2},
\end{aligned}
\tag{30}
$$

where s is the Guass point from interval $(-1,1)$, the relation of θ and $\bar{\theta}$ can be found in Equation (19).

4.3 Numerical quadrature

In numerical implementation, Gaussian rule is applied in both radial and angular direction. 6 Gauss points are used in the radial direction. 18 Gauss points are used in angular direction of each sub-triangle for conformal SST unless specified particularly. For each non-singular element, an adaptive subdivision scheme is used according to the relative distance between the element and collocation point. All the rules are used imperially without any error control algorithm.

5 Crack growth

The approaches used to represent and track the crack propagation can be classified into two manifolds, the implicit method and the explicit method. A typical application of the former method would be the level set method [71] which is coupled in the XFEM/GFEM to represent and evolve the discontinuity [10][11]. The level set function is a signed distance function to the crack surface defined on the underlying mesh, which could be consistent with the mesh discretization of the problem or be independent structured mesh. Since the cracks are open surfaces, one more level set function which should be defined perpendicular to the crack surface is required in order to describe the crack front. The quality to represent the crack surface depends on the resolution of the underlying mesh. Accurately describing the crack surface usually introduces additional computational expense [72]. Advection-type equations should

be solved so as to update the crack front when the crack evolves [73] which increases the computational effort. Chopp and Sukumar [74] proposed the fast marching method to update the crack front location, thus facilitating the process of updating the crack surface [9]. Fries and Baydoun [75] proposed an implicit-explicit method, in which the level set represented crack is explicitly dicretized by triangular facets. Idea shared analogous purpose would be the vector level set method [17]. These methods take advantage of the level set representation for the PU enrichment while avoiding to update the crack surface by solving the equations. Additionally, sharp turns and kinks can be retained by use of explicit crack surfaces rather than pure level sets.

The latter method uses sets of triangular or quadrilateral facets to discretize the crack surface directly. For finite element based methods, the crack evolution process is usually companied with automatic re-meshing operation. For XFEM/GFEM applications, the subdivision of the 3D solid elements needs to be performed for the integration purpose. Both will rely on well-developed meshing/re-meshing packages [76][77]. The explicit representation of crack surfaces by triangulation has been used in meshfree methods as well [16]. It should be noted that this representation method usually results in C^0 crack surface and the crack fronts are composed of line segments. This will lead to at least two shortcomings: (1) the crack front is not captured exactly in computational aspect and this will give inaccuracy in the extraction of the fracture parameters (for example the SIFs) from the numerical solution and geometry approximation error will be accumulated with the crack growth; (2) the local crack front coordinate system is not well defined and the deflection angle is discontinuous, resulting in the non-unique branch enrichment for some local tip center on the crack front, unless the branch enrichment is abandoned [18]. As a remedy, the crack fronts need to be smoothed through some numerical techniques [76][77]. Similar scenario occurs in Lagrange based BEM for fracture modeling. Besides, Paluszny and Zimmerman [78] point out that large numbers of facets are needed in order to more accurately represent the crack surface and the storage increases rapidly with respect to the area of the crack surface when crack propagates. Hence they propose the use of parametric surface, i.e. the NURBS patch, to describe the crack propagation. In their approach, the crack growth is realized geometrically by deforming the NURBS surface through the mid-range La-Greca algorithm [79] to move the control points. Due to the parametrization of the NURBS patch, the crack tip can be sampled anywhere along the crack front, thus the storage for crack

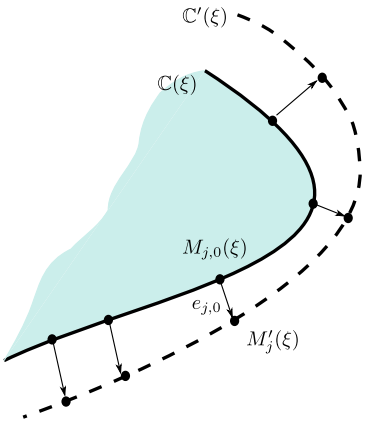

Figure 3: Crack front updating. $\mathbb{C}(\xi)$ is the old crack front curve, $\mathbb{C}'(\xi)$ is the new crack front curve after iteration

discretization increases mildly. Meanwhile the local crack front coordinate system is established on the smooth geometry. However, this method based on re-meshing the finite elements. The mesh regeneration needs to be carefully controlled to ensure the mesh quality. Recently Tambat *et al* proposed an explicitly represented lower-dimension geometry features by NURBS [60][61] through the partition of unity approximation. Instead of using level sets, the lower-dimension features such as cracks are accurately described through the calculation of the distance field in an efficient non-iterative way, providing a promising alternative to evolve discontinuity in the IGAFEM framework. However, more suitable numerical quadrature scheme is desired in order to fully exploit the exact representation in geometry.

In the present work, we use NURBS patches to descretize the crack surfaces. The crack front is exactly described and the local crack tip system is defined naturally and uniquely based on the NURBS patch. Meanwhile, the physical quantities are also approximated by the NURBS basis in the spirit of isogeomtric analysis. Combining with BEM, the smoothness in geometry and stress solution is fully exploited to calculate the fracture parameters and evolve the crack in a stable manner.

5.1 Crack surface updating algorithm

Crack propagation is realized geometrically by advancing the crack front so that the new crack front curve $\mathbb{C}'(\xi)$ shall pass through the new positions of the sample points on the old crack front curve $\mathbb{C}(\xi)$ which is parameterized by the knot vector $\Xi = \{\xi_1, \xi_2, ..., \xi_{n+p+1}\}$, n is the number of basis functions. We define the sample points on $\mathbb{C}(\xi)$ to be $M_j = M(\xi_j), j = 0, 1, ..., N-1$,

and the set of corresponding new positions to be M'_j. The N new positions of sample points are served as the constraints during the deformation process from $\mathbb{C}(\xi)$ to $\mathbb{C}'(\xi)$, and we set $N = n$ here. We adopt the algorithm described in [79]. In this algorithm, the deformation of a curve under multiple constraints is a iteration process. For t-th iterating step, we define the error vector as:

$$e_{j,t} = \overrightarrow{M_{j,t}M'_j}. \tag{31}$$

If $\|\mathbf{e}_t\| < tol$, the iteration ceases and the new crack front curve is obtained ($tol = 1.e-4$ in this work).

To update the control points $P_i, i = 0, 1, ..., n-1$, we define a movement vector $\mathbf{m}$ such that in t-th iterating step:

$$P_{i,t} = P_{i,t-1} + m_{i,t} \tag{32}$$

The movement vector $\mathbf{m}_t$ can be computed as:

$$m_{i,t} = \frac{1}{N}\sum_{j=0}^{N-1} f_{ij}e_{j,t-1}, \tag{33}$$

where $\mathbf{f}_j = \mathbf{f}(\xi_j)$ are the influence functions corresponding to each constraint M'_j. We choose the influence functions to be the NURBS basis functions which are used to describe the curve, i.e. $\mathbf{f}_j = \mathbf{R}_j$. To make sure the influence functions $f_{ij} = f_i(\xi_j)$ associated with each constraint M'_j are linearly independent (so that the constraint is effective to the deformation of the curve), the parameter coordinate ξ_j of each M_j should satisfy $\xi_j \in [\xi_i, \xi_{i+p+1}]$. Thus we use the Greville Abscisse to generate the sample points.

Finally, the error vector is calculated in a recursive way:

$$e_{j,t} = e_{j,t-1} - \frac{1}{N}\sum_{k=0}^{N-1}\langle \mathbf{R}_j, \mathbf{f}_k\rangle e_{k,t-1} \tag{34}$$

The details for updating the crack front is given in Algorithm (1). Once the new crack front curve is obtained, the new crack surfaces can be generated by lofting along the crack extension direction from the old curve to the new curve. The generated crack surfaces shall be merged into the old crack surfaces with C^0 joint or C^1 joint. In this work C^0 merge is adopted.

Algorithm 1 Crack front updating algorithm

Data: old crack front curve $\mathbb{C}(\xi)$; sample points M_j; new positions of sample points M_j'
Result: new crack front curve that passes through all M_j'
$t = 0$;
$tol = 1.e-4$;
$e_{j,0} = \overrightarrow{M_{j,0}M_j'}$;
while $\|\mathbf{e}_t\| > tol$ **do**
  $t = t + 1$;
  $m_{i,t} = \frac{1}{N}\sum_{j=0}^{N-1} f_{ij}e_{j,t-1}$;
  $P_{i,t} = P_{i,t-1} + m_{i,t}$;
  $e_{j,t} = e_{j,t-1} - \frac{1}{N}\sum_{k=0}^{N-1}\langle \mathbf{R}_j, \mathbf{f}_k\rangle e_{k,t-1}$;
end

5.2 Computation of stress intensity factors

The driving force for the evolution of fatigue fracture is characterized by some fracture parameters such as the stress intensity factors (SIFs), which can be extracted from the numerical solution. If the fracture parameters are computed based on the point-wise tips on the crack front independently, it can be regarded as a local approach. The key factor to compute accurately the SIFs in the local approach is to avoid the discretization and path dependence as much as possible. Various methods have been developed to extract the SIFs in the framework of FEM and BEM. The displacement correlation method [80], with or without the crack-tip singular element, is a simple and fast way for this aim. Nevertheless, The path dependence of this method can not be neglected and an extrapolation technique is performed upon a group of calculations. The virtual crack extension method (VCE) [81][82], was applied to compute SIFs based on the calculation of the released strain energy per a virtual crack extension. The original VCE relies on the construction of structured mesh along the crack front, which increases the mesh burden. however it should be noted that the variational form of the strain energy which involves the energy release rate and the crack extension has been applied for automatic crack growth [83][84] where the crack extension is assigned with physical interpretation. This method minimize the strain energy in a global sense, thus leading to a significant difference from local approach and has recently been investigated in the framework of XFEM [85].

The virtual crack closure integral (VCCI) method is proposed based on the virtual crack extension, is another alternative to extract SIFs in linear elastic fracture. Due to the simplicity and accuracy, the VCCI has been widely used in FEM and BEM [86]. While it should be noted

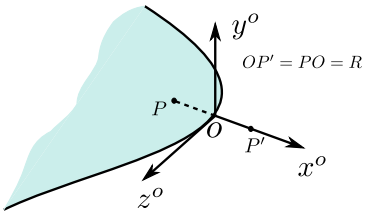

Figure 4: Crack tip coordinate system

that this method requires the element near the crack front aligned in consistence with the normal direction of the crack front. The path-independent J integral proposed by Rice [87] is an attractive method due to its robustness regarding the relative independence in discretization and path of integral. The method soon was extended into many branches and achieve good results in both FEM and BEM [88][89][90][91][92]. The contour J integral is advised to cast into the equivalent domain integral form in FEM as the nodal stress is not straightforward solution and requirement in mesh discretization is relaxed. While in BEM the contour definition can be adopted directly [93]. In order to extract mixed mode SIFs, different techniques are developed. The J_x integrals ($x = 1, 2, 3$), as the components of **J** integral, can be directly used to evaluate the SIFs. However, the evaluation of J_2 and J_3 (or G_{III}) exhibits numerical difficulty due to the singularity [94]. The J_1 integral (or J integral) can also been used to extract mixed mode SIFs, with some auxiliary operation. One way is to decompose the displacement and stress fields into symmetric and antisymmetric portions with structured mesh along the crack front, then three modes of J integral can be calculated directly [95][96][97][98]. The other method named M integral (or interaction energy integral), was developed by introducing asymptotic fields as the auxiliary solution [89] has been extended in (X)FEM [99][11] and BEM [100].

Both the VCCI and contour M integral have been investigated for the calculation of SIFs in the fracture analysis via 3D isogeometric BEM. The point-wise crack tip coordinate system is established along the crack front as in Figure 4. The physical quantities are all in the crack tip local coordinate system thus the superscript 'o' is omitted in this section.

5.2.1 Contour M integral

The definition of J_k integral stems from two dimensions as:

$$J_k := \lim_{\Gamma_\epsilon \to 0} \int_{\Gamma_\epsilon} (W\delta_{jk} - \sigma_{ij} u_{i,k}) n_j \mathrm{d}\Gamma = \lim_{\Gamma_\epsilon \to 0} \int_{\Gamma_\epsilon} P_{kj} n_j \mathrm{d}\Gamma, \quad k = 1, 2 \tag{35}$$

where P_{kj} is the Eshelby tensor, $W = 1/2\sigma_{ij}\epsilon_{ij}$ is the strain energy density. Γ_ϵ is a small contour with radius R centred at crack tip 'o' in the '$x_o - y_o$' plane and n_j is the unit outward normal of Γ_ϵ.

It can be extended to three dimensional point-wise definition by taking a tubular surface around the crack front. When the contour Γ_ϵ is small enough, the plane strain condition is approximately satisfied. We could use the contour definition directly on the premise that a small contour is assumed.

It is known that the J integral (J_1) and the SIFs have the relationship

$$J = G_I + G_{II} + G_{III} = \frac{1-\nu^2}{E}K_I^2 + \frac{1-\nu^2}{E}K_{II}^2 + \frac{1}{2\mu}K_{III}^2, \tag{36}$$

where G_i and K_i ($i = I, II, III$) are the energy release rates and SIFs for the three modes of fracture.

By applying the J integral under two states, one the real state (denoted with superscript '1'), the other the auxiliary state (superscript '2'), then adding them together, the mixed term M can be obtained:

$$J^{(1+2)} = \int_{\Gamma_\epsilon} \Big[0.5(\sigma_{ij}^{(1)} + \sigma_{ij}^{(2)})(\epsilon_{ij}^{(1)} + \epsilon_{ij}^{(2)})\delta_{1j} - (\sigma_{ij}^{(1)} + \sigma_{ij}^{(2)})\frac{\partial(u_i^{(1)} + u_i^{(2)})}{\partial x_1}\Big]n_j \mathrm{d}\Gamma \tag{37}$$

Rearranging the two state terms gives

$$J^{(1+2)} = J^{(1)} + J^{(2)} + M^{(1,2)} \tag{38}$$

where

$$M^{(1,2)} = \int_{\Gamma_\epsilon} \Big[W^{(1,2)}\delta_{1j} - \sigma_{ij}^{(1)}\frac{\partial u_i^{(2)}}{\partial x_1} - \sigma_{ij}^{(2)}\frac{\partial u_i^{(1)}}{\partial x_1}\Big]n_j \mathrm{d}\Gamma \tag{39a}$$

$$W^{(1,2)} = \sigma_{ij}^{(1)}\epsilon_{ij}^{(2)} = \sigma_{ij}^{(2)}\epsilon_{ij}^{(1)} \tag{39b}$$

Combined with Equation (36), the following relationship can be obtained for the M integral,

$$M^{(1,2)} = \frac{2(1-\nu^2)}{E}(K_I^{(1)}K_I^{(2)} + K_{II}^{(1)}K_{II}^{(2)}) + \frac{1}{\mu}K_{III}^{(1)}K_{III}^{(2)}. \tag{40}$$

Then SIFs can be extracted respectively, for example, let state 2 be the pure mode III asymp-

totic fields with $K_I^{(2)} = 0$, $K_{II}^{(2)} = 0$, $K_{III}^{(2)} = 1$ and K_{III} in real state 1 can be found as

$$K_{III}^{(1)} = \mu M^{(1,\text{ mode } III)} \tag{41}$$

K_I and K_{II} can be given in a similar fashion. Here the first order asymptotic displacement and stress solutions (see Appendix B) are selected as the auxiliary fields.

5.2.2 Virtual crack closure integral

In the VCCI, the strain energy release rate is equal to the work done by closing the virtual crack extension. Three modes of the strain energy release rate are given by

$$\begin{aligned} G_I &= \frac{1}{2R}\int_0^R \sigma_{yy}(x)[\![u_y(R-x)]\!]\mathrm{d}x, \\ G_{II} &= \frac{1}{2R}\int_0^R \sigma_{xy}(x)[\![u_x(R-x)]\!]\mathrm{d}x, \\ G_{III} &= \frac{1}{2R}\int_0^R \sigma_{yz}(x)[\![u_z(R-x)]\!]\mathrm{d}x, \end{aligned} \tag{42}$$

where $OP' = R$ is the virtual crack advance. For the evaluation of $[\![u_j(R-x)]\!]$ on PO, the point inversion algorithm needs to be performed in order to find the parametric coordinate in the crack modeled by NURBS surface [66]. The domains of these integrals OP' and PO are dicretized by single linear element [101]. And the R is identical for all the crack tips. Then K_I, K_{II} and K_{III} can be computed according to Equation (36).

5.3 Paris law

The Paris-based laws have been used to describe the steady state crack growth in the fatigue failure process. We use the original Paris law as follows:

$$\frac{\mathrm{d}a}{\mathrm{d}N} = C(\Delta K)^m, \tag{43}$$

where N denotes the number of load cycles. C and m are the material parameters. ΔK is the SIF range. For mixed mode crack, the K is taken as the equivalent SIF K_{eq} which is given as [5]:

$$K_{eq} = \sqrt{K_I^2 + K_{II}^2 + (1+\nu)K_{III}^2} \tag{44}$$

We specify the maximum crack advance Δa^{max} so that the number of load cycles can be obtained according to the law. It should be noted that the crack propagation velocity could be varied for the crack tips along the front. In a single propagation step, the crack advance for each crack tip is regularized by the Δa^{max},

$$\Delta a^i = C(\Delta K_{eq}^i)^m \frac{\Delta a^{max}}{C(\Delta K_{eq}^{max})} = \Delta a^{max} \Big(\frac{\Delta K_{eq}^i}{\Delta K_{eq}^{max}} \Big)^m. \tag{45}$$

The maximum hoop stress criterion is used to determine the direction of crack propagation. We assume that the crack propagates in the direction θ_c such that the hoop stress is maximum, which is given by the following expression [102]

$$\theta_c = 2\text{arctan} \left[\frac{-2(K_{II}/K_I)}{1 + \sqrt{1 + 8(K_{II}/K_I)^2}} \right]. \tag{46}$$

6 Numerical examples

In this section, numerical examples about the penny-shaped crack and elliptical crack will be given, modeled in infinite domain with the COD equation (10) and in finite domain with the dual equations (6) and (7). The convergence in COD is compared and the numerical SIFs are calculated by both VCCI and M integral. Then the crack growth algorithm is checked. The Young's modulus $E = 1000$ and Poisson's ratio $\nu = 0.3$ for all the cases.

6.1 Penny-shaped crack

Suppose a penny-shaped crack is subjected to the remote tension σ_0, i.e. $\mathbf{t}^\infty = (0, 0, \sigma_0)$. The radius of circle is a. The inclination angle is φ and circular angle θ is defined in the crack plane (Oxy) as in Figure 5. The analytical solution of SIFs reads:

$$\begin{aligned} K_I &= \frac{2}{\pi} \sigma_0 \sqrt{a\pi} \cos^2 \varphi, \\ K_{II} &= \frac{4}{\pi(2-\nu)} \sigma_0 \sqrt{a\pi} \cos\varphi \sin\varphi \cos\theta, \\ K_{III} &= \frac{4(1-\nu)}{\pi(2-\nu)} \sigma_0 \sqrt{a\pi} \cos\varphi \sin\varphi \sin\theta. \end{aligned} \tag{47}$$

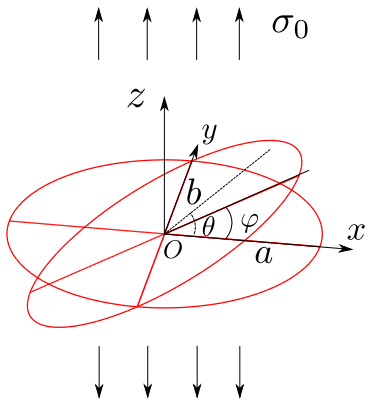

Figure 5: Geometry for penny-shaped crack ($a = b$) and elliptical crack ($a \neq b$)

In particular, when the crack plane is horizontal ($\varphi = 0$), the analytical normal displacement is given as:

$$u_z(r, \theta, 0) = \frac{2(1-\nu)\sigma_0}{\pi\mu}\sqrt{a^2 - r^2}, \quad r \leqslant a. \tag{48}$$

6.1.1 Singular integration test

The problem is modeled by COD equation (10), so that only a single NURBS patch is used to represent the crack, and the numerical COD will be compared with the analytical solution. The collocation points are moved aside from the pole in order not to locate at the degenerated point. The NURBS basis functions associated with the pole, however, are enforced to C_0 through the corresponding control points sharing the same degrees of freedom. The BIEs from these moved collocation points are merged to one equation.

We note that the COD solution only varies in radial direction while keeping the same in angular direction, thus 4 elements are used in angular direction. This will lead to high aspect ratio of each element with the refinement in radial direction. Figure 6 compares the L_2 norm error in COD for $\varphi = 0$. 'ngp_s' denotes the number of Gauss points in angular direction in each sub-triangle. original SST means a direct use of the method and improved SST denotes the SST with conformal mapping. It can be observed that

- when ngp_s= 30, the original SST and improved SST get comparable error. However, the error from original SST is non-uniformly distributed whilst the improved SST gets a more uniform error distribution;

- when ngp_s= 18, the error from original SST gets diverged (e_{L_2} =1.467716e-1), while improved SST keeps the same accuracy as it from ngp_s= 30;
- the error becomes big near the crack front. This is due to the crack tip singularity.

Thus we conclude that original SST need more Gauss points in order to get a reasonable accuracy. If we move the knot ($\eta = 0.875$) next to the crack front in radial direction closer to the crack front ($\eta = 0.94$) and repeat comparison as in Figure 7. We find that even ngp_s= 30, original SST still gives big error. while the improved method shows a higher accuracy than before. We can refer that, due to the crack tip singularity, a refined mesh near the crack front should give better accuracy in COD, but the original SST is sensitive to the element distortion and gives diverged results. The improved SST presents a robust application for this kind of mesh configuration.

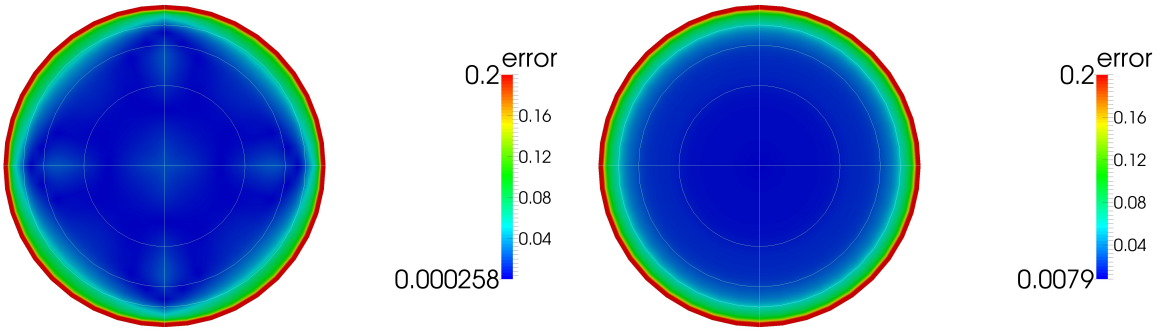

(a) original SST, ngp_s=30, e_{L_2} =3.344418e-2 (b) improved SST, ngp_s=30, e_{L_2} =3.844282e-2

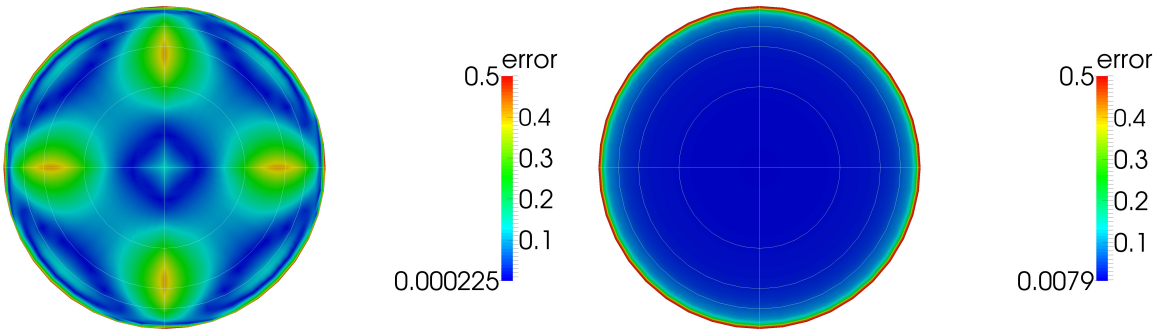

(c) original SST, ngp_s=18, e_{L_2} =1.467716e-1 (d) improved SST, ngp_s=18, e_{L_2}=3.844282e-2

Figure 6: Error in crack opening displacement for penny crack. 'ngp_s' denotes the number of Gauss points in angular direction in each sub-triangle. Knot vectors: angular direction $\boldsymbol{\xi}$=[0,0,0,0.25,0.25,0.5,0.5,0.75,0.75,1,1,1], radial direction $\boldsymbol{\eta}$=[0,0,0,0.5,0.75,0.875,1,1,1]

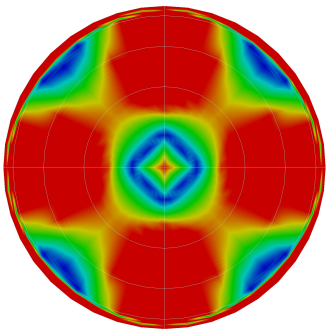

(a) original SST, ngp_s=30, e_{L_2}=8.138911e-1

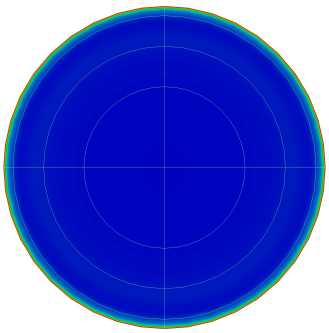

(b) improved SST, ngp_s=30, e_{L_2}=1.755681e-2

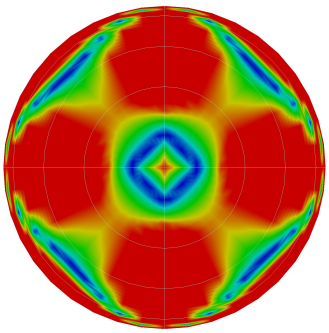

(c) original SST, ngp_s=18, e_{L_2}=7.110011e-1

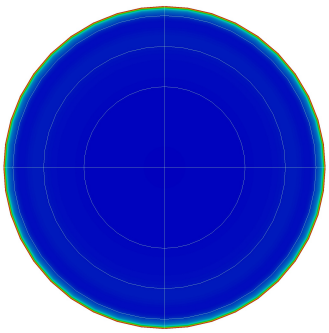

(d) improved SST, ngp_s=18, e_{L_2}=1.755679e-002

Figure 7: Error in crack opening displacement for penny crack. Knot vectors: angular direction $\boldsymbol{\xi}$=[0,0,0,0.25,0.25,0.5,0.5,0.75,0.75,1,1,1], radial direction $\boldsymbol{\eta}$=[0,0,0,0.5,0.75,0.94,1,1,1]

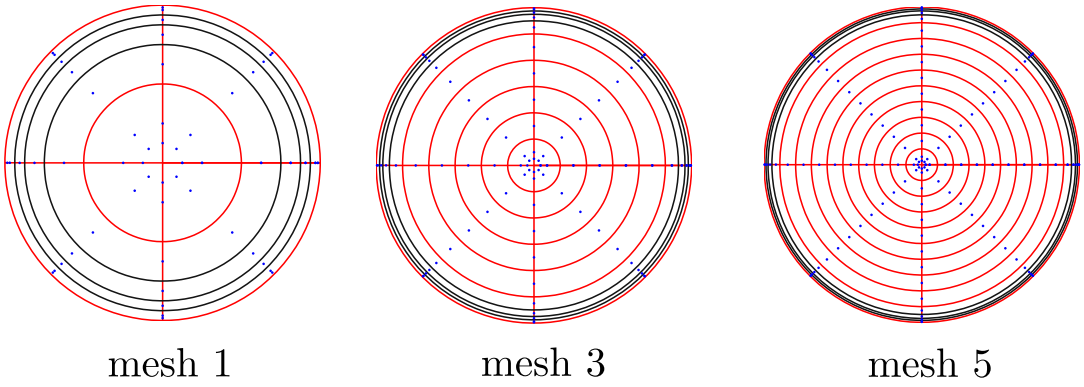

Figure 8: NURBS($p = q = 2$) represented crack surface meshes with 1, 5, and 9 uniformed refinement in radial direction, followed by graded refined elements (with black edges) close to crack front. The blue dots are collocation points

6.1.2 Convergence test

Uniform mesh refinement in the parametric space is performed and we calculate the element size h as $h = \sqrt{S_e^{max}}$, where S_e^{max} denotes the maximum area of the element. The convergence curve is plotted in Figure 9 where we compared both the quadratic and cubic NURBS basis functions. It can be concluded that the degree elevation helps to improve the accuracy. But the order of convergence rate (oc) keeps almost the same value ($oc = 1$). The deterioated oc is due to the physical singularity along the crack front.

As stated in the above section, the uniform refinement is not an efficient way to improve the accuracy for penny crack. Thus five mesh configurations are designed through keeping the element number in angular direction while the mesh is uniformly refined with the element number 2, 4, 6, 8 and 10 in radial direction, then the element at crack front is further gradely refined via a consecutive knot insertion in order to reduce the error caused by crack tip singularity (Figure 8 shows mesh 1, 3 and 5). Figure 10 plots the result for convergence study. It can be seen that the accuracy is improved almost by one order and the final estimate convergence rate is two times higher than the uniform refinement. This indicates the efficiency of IGABEM in the application of fracture simulation.

6.1.3 Stress intensity factor test

In this subsection, the computation of SIFs is checked. Instead of using COD equation to model the penny-shaped crack in the infinite domain, we put two overlapped crack surfaces in a cube

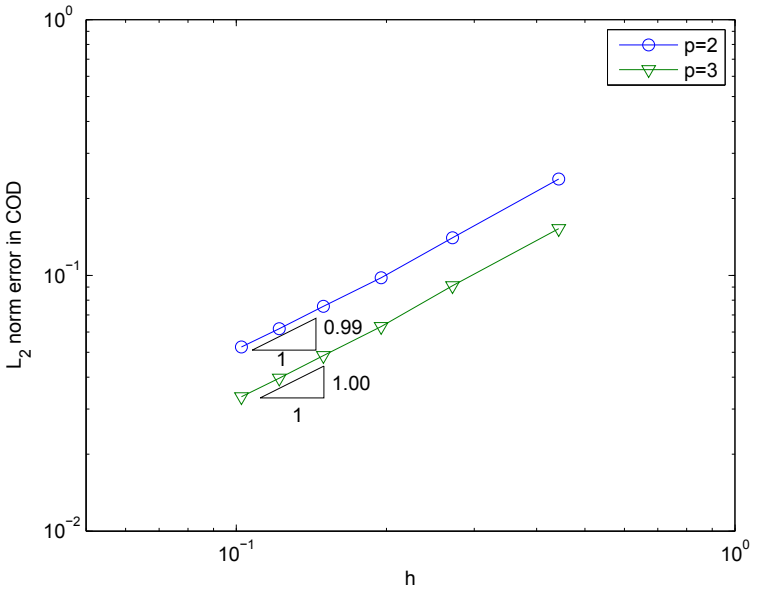

Figure 9: L_2 norm error of COD for penny-shaped crack

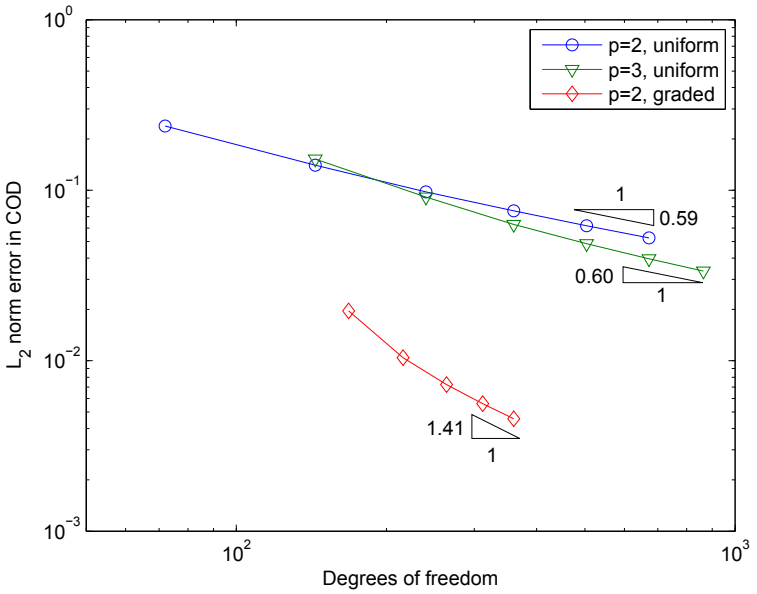

Figure 10: L_2 norm error of COD for penny-shaped crack

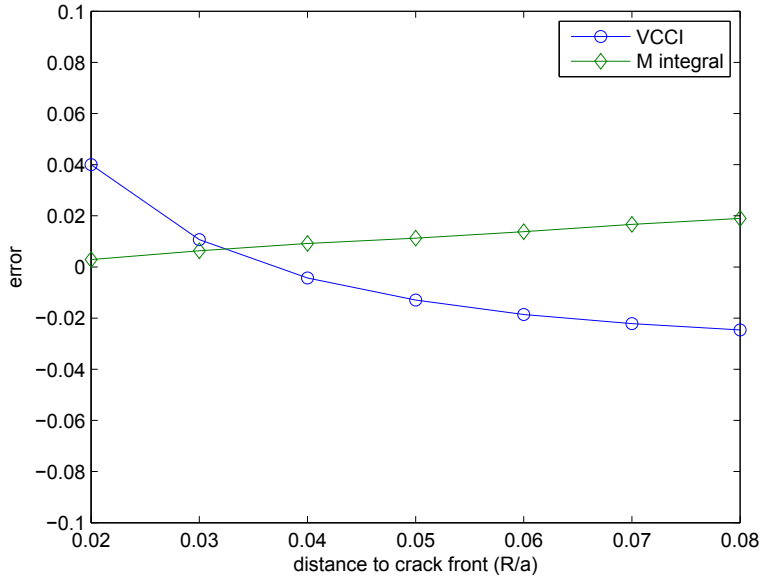

Figure 11: Path independence check for VCCI and M integral

with size $L = 200a$ such that we could compare the numerical SIFs with the analytical solution for infinite domain. Dual equations are used for this case.

Figure 11 investigates the path independence of the M integral and VCCI for mode I penny-shaped crack. Here 'R' denotes the virtual crack advance in VCCI and the radius of the contour in M integral. It can be seen that when R/a is from 0.02 to 0.08, both methods show path dependent behavior. For M integral, the error varies within 2%. When the radius of contour is small, K_I converges to analytical value; while increasing R, since the stress field for the crack tip is influence by other tips in the crack front, plane strain condition is not satisfied properly, the method becomes inaccurate. For VCCI, the error varies within 6% and generally a small virtual crack advance is needed. However, if R is too small, difficulty in numerical evaluation of stress and COD close to crack front will arise which lead to the inaccuracy of K_I. From the figure we can also refer that M integral presents a smaller reduction in error than VCCI.

Figure 12 compares the SIFs obtained from M integral with $R = 0.02a$ and VCCI with $R = 0.04a$ for the mixed mode penny-shaped crack with inclination angle $\varphi = \pi/6$. It is seen that both methods agree well with the analytical solution. K_{III} from M integral shows deviation near $\theta = \pi/2$ and $3\pi/2$. Table 1 presents the error at $\theta = 0$, $\pi/4$ and $\pi/2$. It can be observed that the error of K_I and K_{II} is within 1% by both methods, while within 7% for K_{III} by M integral. we can conclude that the IGABEM can provide accurate SIFs, and the numerical

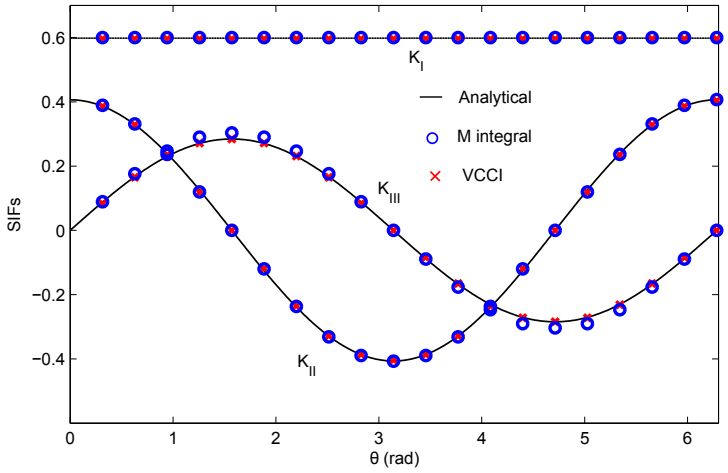

Figure 12: Stress intensity factors for penny crack with $\varphi = \pi/6$

SIFs along crack front is quite smooth, although with only 4 elements in angular direction and without any smoothness operation. This gives the premise for a stable evolution for the crack growth simulation.

	K_{II}		K_{III}	
	VCCI	M integral	VCCI	M integral
$\theta = 0$	7.133e-3	2.008e-3	2.898e-8	5.221e-9
$\theta = \pi/4$	7.167e-3	1.983e-3	1.591e-4	6.243e-2
$\theta = \pi/2$	1.622e-8	1.228e-8	2.010e-4	1.894e-2

Table 1: Error of SIFs for penny-shaped crack with $\varphi = \pi/6$.

6.2 Elliptical crack

Suppose an elliptical crack is subjected to the remote tensile loading σ_0 in the normal direction, i.e. $\mathbf{t}^\infty = (0, 0, \sigma_0)$. The semi-major axes is a, semi-minor axes b. The inclination angle is φ and elliptical angle θ is defined in the crack plane as in Figure 5. The analytical solution of

SIFs reads:

$$
\begin{aligned}
K_I &= \frac{\sigma_0}{2}(1+\cos 2\varphi)\frac{\sqrt{b\pi}f(\theta)}{E(k)},\\
K_{II} &= \frac{\sigma_0}{2}\sin 2\varphi\frac{\sqrt{b\pi}k^2(b/a)\cos\theta}{f(\theta)B(k)},\\
K_{III} &= \frac{\sigma_0}{2}\sin 2\varphi\frac{\sqrt{b\pi}k^2(1-\nu)\sin\theta}{f(\theta)B(k)},\\
k^2 &= 1-\frac{b^2}{a^2},\\
f(\theta) &= (\sin^2\theta+\frac{b^2}{a^2}\cos^2\theta)^{1/4},\\
B(k) &= (k^2-\nu)E(k)+\nu\frac{b^2}{a^2}K(k),
\end{aligned}
\tag{49}
$$

where $K(k)$ and $E(k)$ are elliptical integrals of the first kind and second kind, respectively:

$$
\begin{aligned}
K(k) &= \int_0^{\pi/2}\frac{1}{\sqrt{1-k^2\sin^2\theta}}\mathrm{d}\theta,\\
E(k) &= \int_0^{\pi/2}\sqrt{1-k^2\sin^2\theta}\mathrm{d}\theta.
\end{aligned}
\tag{50}
$$

In particular, when $\varphi = 0$, the displacement in the crack normal direction reads:

$$
u_z(x,y,0) = \frac{2(1-\nu)\sigma_0}{\mu}\frac{b}{E(k)}\sqrt{1-\frac{x^2}{a^2}-\frac{y^2}{b^2}}. \tag{51}
$$

The difference of the elliptical crack and penny crack is that the mode I SIF is not a constant, due to the variation of curvature along the crack front. The problem is modeled by COD equation (10) and mesh configuration and collocation is analogous to penny-shaped crack. The tip in numerical aspect is, for elliptical crack, the elements have high element aspect ratio as well as non-orthogonal basis vectors. Figure 13 shows that original SST presents erroneous result with 18 Gauss points in angular direction. While the improved SST gives a reasonable COD and error distribution.

For the convergence study, we first give the result of uniform refinement in parametric space in Figure 15. Then the same graded mesh configurations for elliptical crack are generated as done for penny crack as in Figure 14. Figure 16 compares the result between uniform mesh and graded mesh. The convergence feature is almost the same as that of penny crack. And we can conclude that the IGABEM also suits well for modeling elliptical crack.

For the test of SIFs computation, we put two overlapped crack surfaces in a cube with size

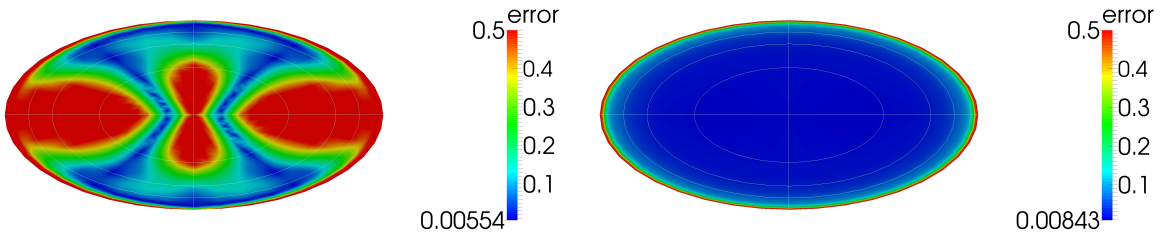

(a) original SST, ngp_s=18, e_{L_2}=4.603473e-1 (b) improved SST, ngp_s=18, e_{L_2}=3.798002e-2

Figure 13: Error in crack opening displacement for elliptical crack. Knot vectors: angular direction $\boldsymbol{\xi}$=[0,0,0,0.25,0.25,0.5,0.5,0.75,0.75,1,1,1], radial direction $\boldsymbol{\eta}$=[0,0,0,0.5,0.75,0.875,1,1,1]

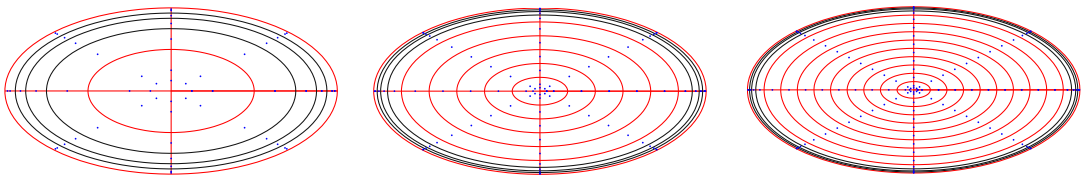

mesh 1 mesh 3 mesh 5

Figure 14: NURBS($p = q = 2$) represented crack surface meshes with 1, 5, and 9 uniformed refinement in radial direction, followed by graded refined elements (with black edges) close to crack front. The blue dots are collocation points

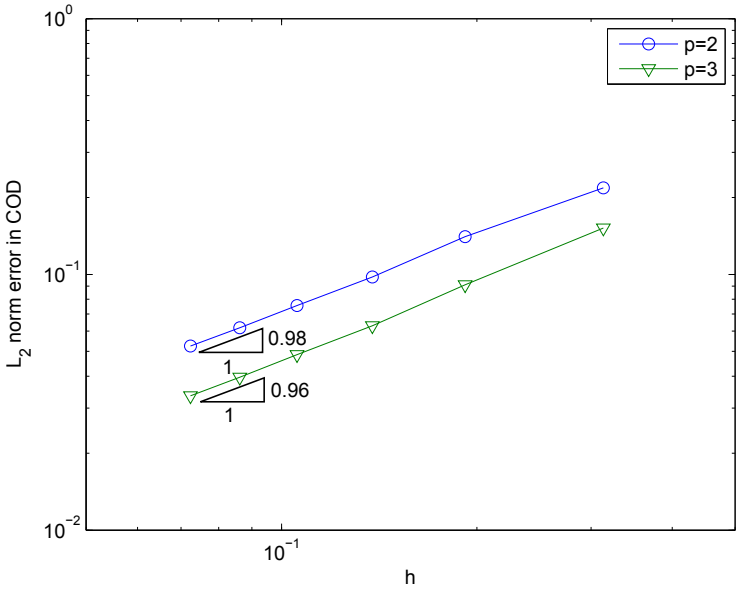

Figure 15: L_2 norm error of COD for elliptical crack

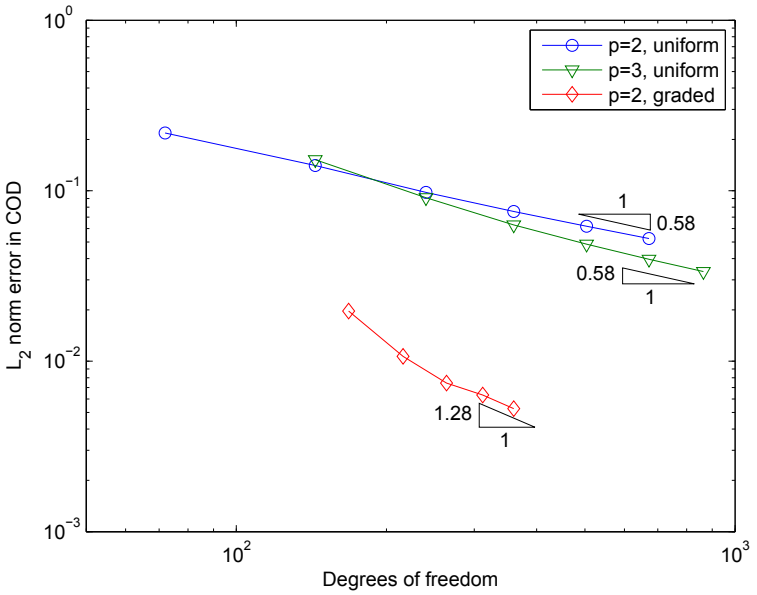

Figure 16: L_2 norm error of COD for elliptical crack

$L = 200a$ such that we could compare the numerical SIFs with the analytical solution for infinite domain. Dual equations are used. Figure 17 compares the SIFs obtained from M integral with $R = 0.02b$ and VCCI with $R = 0.02b$ for the mixed mode elliptical crack with inclination angle $\varphi = \pi/6$. Table 2 presents the error at $\theta = 0$ and $\pi/2$ for the SIF in three modes. It can be seen that the error for all the SIFs is within 7%. And the SIFs along the crack front is smooth. We note that the SIFs accuracy of elliptical crack is a bit worse than penny crack, which is due to the varied curvature along the crack front. Since the fixed R is used, the singularity at the sample points near the semi-major and semi-minor axes would be different, which will lead to inaccuracy in SIFs evaluation. More suitable way to estimate the SIFs for elliptical crack would be one of the future work.

	K_I		K_{II}		K_{III}	
	VCCI	M integral	VCCI	M integral	VCCI	M integral
$\theta = 0$	4.564e-2	1.534e-2	4.138e-2	1.279e-2	1.226e-7	2.174e-7
$\theta = \pi/2$	8.284e-3	2.214e-2	6.936e-8	5.152e-8	6.882e-3	5.959e-2

Table 2: error of SIFs for elliptical crack with $\varphi = \pi/6$

6.3 Fatigue crack growth

In this section, the crack surface updating algorithm is tested combined with the Paris law. We fist check the crack growth of the horizontal penny crack under the uniform tension from

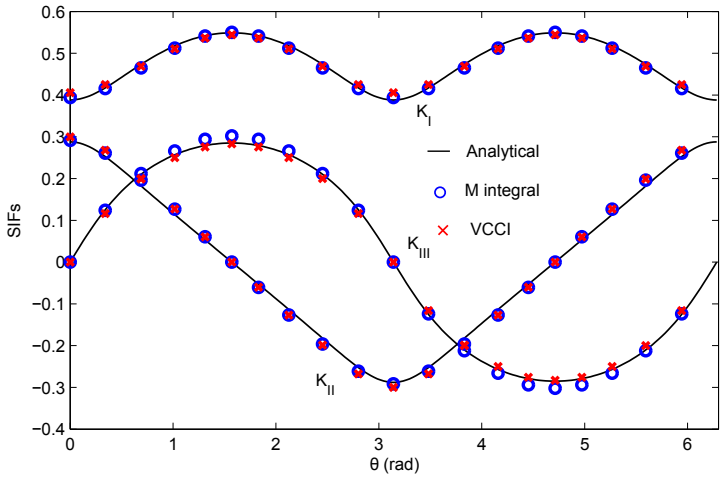

Figure 17: Stress intensity factors for elliptical crack with $\varphi = \pi/6$

section 6.1.3. The fatigue parameters $m = 2.1$ and the specified $\Delta a_{max} = 0.2a$. We propagate 10 steps and make a comparison with the exact result and the result from the XFEM+level set method [103] as in Figure 18(a) and (b). It can be observed that the crack front for each step agrees well with exact solution by IGABEM, while the crack front deviates gradually from the exact solution with the crack growth by XFEM+level set method, due to the fact that the level set method is restricted in describing the crack front exactly and this inaccuracy will be accumulated step by step. We then compute the crack propagation for $m = 5$, and the result is presented in Figure 18 (c). We find that the numerical crack front still agrees well with the exact front, although the high index value is supposed to exaggerate the error of velocities of the sample points. This test shows the proposed crack propagation scheme owns the ability to evolve the crack in a stable manner, thanks to the smoothness in the numerical stress and SIFs solution and exact representation in crack evolution. Finally, we simulate the crack growth for elliptical crack with inclination angle $\varphi = \pi/6$ modeled by the dual equations in finite domain taken from section 6.2. Figure 19 illustrates the 1, 5 and 10th of the propagation step.

7 Conclusions

The formulation and implementation of isogeometric boundary element methods (IGABEM) for simulating 3D fatigue fracture problem are outlined in this paper. The same NURBS basis functions are used for the discretization of geometry/crack and the approximation of displace-

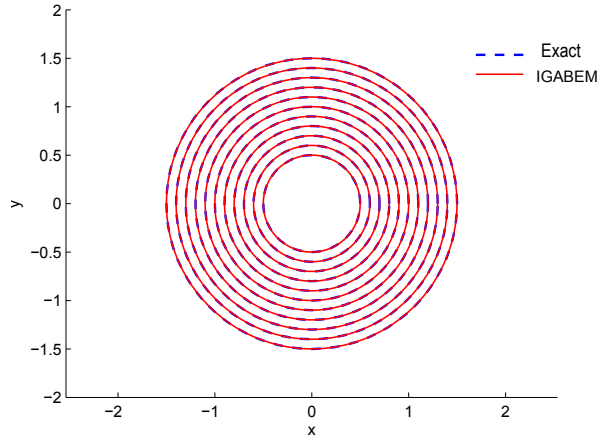

(a) IGABEM, $m = 2.1$

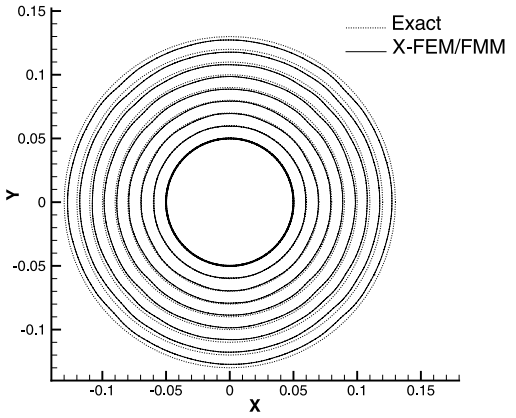

(b) XFEM/FMM, $m = 2.1$, Sukumar *et al* 2003

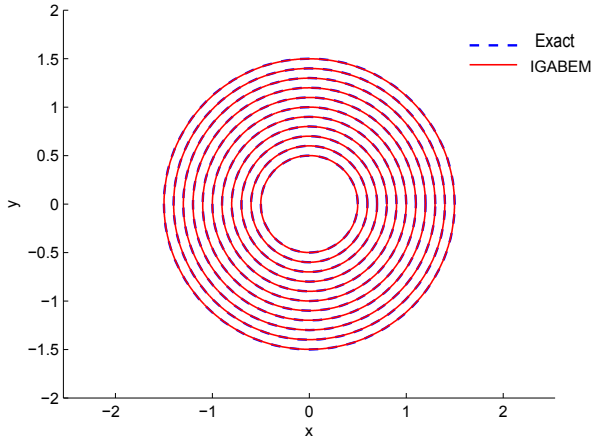

(c) IGABEM, $m = 5$

Figure 18: Fatigue crack growth of the first 10 steps of a penny crack

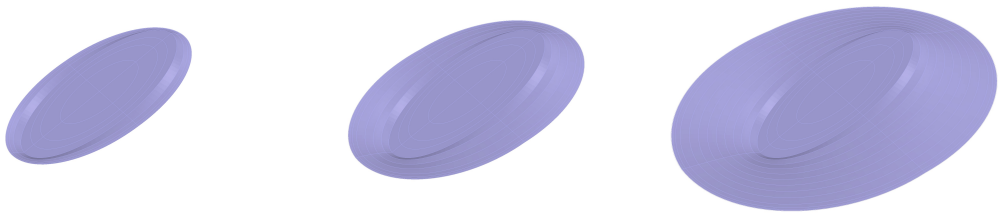

(a) Step 2 (b) Step 5 (c) Step 10

Figure 19: Fatigue crack growth simulation of an elliptical crack

ment/traction in the isogeometric framework. The singularity subtraction technique (SST) proposed in [65] for the treatment of (hyper-)singular integrals in BEM. The improved SST [70] has been extended to quadrilateral element such that it can be applied to tensor-product NURBS basis functions. Both the COD form and dual equations of IGABEM have been realized for the crack modeling. And the two ways to extract SIFs, the contour-based M integral and VCCI, are compared. An algorithm to propagate the NURBS-represented crack surface is presented and validated. The highlights of this work include:

(1) The proposed singular integration scheme can preserve the quadrature accuracy for highly distorted elements which exist commonly in IGA. Thus it enables a robust IGABEM implementation;

(2) By selecting the graded mesh refinement in the direction where the crack tip singularity varies, the convergence rate can be improved by 2 times and accuracy can be improved by one order, than the uniform refinement. This shows the efficiency of IGABEM in the application of fracture problem;

(3) The local crack tip system is setup naturally and uniquely thanks to the NURBS representation of the crack surface. Combining with the continuity in stress solution in BEM, the obtained SIFs along the crack front are smooth and accurate;

(4) The proposed algorithm for crack propagation is validated to be stable, even for high index value in Paris law, due to the smoothness in crack front geometry and numerical SIFs.

The future work will focus on the surface cracks problem, where the crack will have intersection with the body geometry. Meanwhile, the fast solution as proposed in [49] is also a point of interest.

Acknowledgements

The first and last authors would like to acknowledge the financial support of the Framework Programme 7 Initial Training Network Funding under grant number 289361 'Integrating Numerical Simulation and Geometric Design Technology'. S. P. A. Bordas also thanks partial funding for his time provided by the UK Engineering and Physical Science Research Council (EPSRC) under grant EP/G069352/1 Advanced discretisation strategies for 'atomistic' nano CMOS simulation; the EPSRC under grant EP/G042705/1 'Increased Reliability for Industrially Relevant

Automatic Crack Growth Simulation with the eXtended Finite Element Method' and the European Research Council Starting Independent Research Grant (ERC Stg grant agreement No. 279578) entitled 'Towards real time multiscale simulation of cutting in non-linear materials with applications to surgical simulation and computer guided surgery'. E. Atroshchenko was partially supported by Fondecyt grant number 11130259 entitled 'Boundary element modeling of crack propagation in micropolar materials'.

Appendix

A The local expansions in SST

Supposing the parametric coordinate $\boldsymbol{\xi}(\xi,\eta)$ is in the knot interval $[\xi_1,\xi_2]\times[\eta_1,\eta_2]$, the mapping between parametric coordinate and parent coordinate is:

$$\begin{aligned}\xi &= \frac{1}{2}(\xi_2-\xi_1)\bar{\xi}+\frac{1}{2}(\xi_2+\xi_1),\\ \eta &= \frac{1}{2}(\eta_2-\eta_1)\bar{\eta}+\frac{1}{2}(\eta_2+\eta_1).\end{aligned} \tag{52}$$

And the Jacobian transformation for this would be:

$$\begin{aligned}\bar{J}_\xi &= \frac{\partial\xi}{\partial\bar{\xi}} = \frac{1}{2}(\xi_2-\xi_1),\\ \bar{J}_\eta &= \frac{\partial\eta}{\partial\bar{\eta}} = \frac{1}{2}(\eta_2-\eta_1),\\ \bar{J}(\boldsymbol{\xi}) &= \bar{J}_\xi\bar{J}_\eta.\end{aligned} \tag{53}$$

The Taylor expansion of $x_i - s_i$ with respect to the source point in the parent space would be:

$$\begin{aligned}x_i-s_i = \Big[\frac{\partial x_i}{\partial\bar{\xi}}\Big|_{\bar{\boldsymbol{\xi}}=\bar{\boldsymbol{\xi}}_s}(\bar{\xi}-\bar{\xi}_s)+\frac{\partial x_i}{\partial\bar{\eta}}\Big|_{\bar{\boldsymbol{\xi}}=\bar{\boldsymbol{\xi}}_s}(\bar{\eta}-\bar{\eta}_s)\Big]+\Big[\frac{\partial^2 x_i}{\partial\bar{\xi}^2}\Big|_{\bar{\boldsymbol{\xi}}=\bar{\boldsymbol{\xi}}_s}\frac{(\bar{\xi}-\bar{\xi}_s)^2}{2}\\ +\frac{\partial^2 x_i}{\partial\bar{\xi}\partial\bar{\eta}}\Big|_{\bar{\boldsymbol{\xi}}=\bar{\boldsymbol{\xi}}_s}(\bar{\xi}-\bar{\xi}_s)(\bar{\eta}-\bar{\eta}_s)+\frac{\partial^2 x_i}{\partial\bar{\eta}^2}\Big|_{\bar{\boldsymbol{\xi}}=\bar{\boldsymbol{\xi}}_s}\frac{(\bar{\eta}-\bar{\eta}_s)^2}{2}\Big]+\cdots.\end{aligned} \tag{54}$$

Note that:

$$\begin{aligned}
\frac{\partial x_i}{\partial \bar{\xi}} &= \frac{\partial x_i}{\partial \xi}\frac{\partial \xi}{\partial \bar{\xi}} = \frac{\partial x_i}{\partial \xi}\bar{J}_\xi, \\
\frac{\partial x_i}{\partial \bar{\eta}} &= \frac{\partial x_i}{\partial \eta}\frac{\partial \eta}{\partial \bar{\eta}} = \frac{\partial x_i}{\partial \eta}\bar{J}_\eta, \\
\frac{\partial^2 x_i}{\partial \bar{\xi}^2} &= \frac{\partial^2 x_i}{\partial \xi^2}\Big(\frac{\partial \xi}{\partial \bar{\xi}}\Big)^2 = \frac{\partial^2 x_i}{\partial \xi^2}\bar{J}_\xi^2, \\
\frac{\partial^2 x_i}{\partial \bar{\eta}^2} &= \frac{\partial^2 x_i}{\partial \eta^2}\Big(\frac{\partial \eta}{\partial \bar{\eta}}\Big)^2 = \frac{\partial^2 x_i}{\partial \eta^2}\bar{J}_\eta^2, \\
\frac{\partial^2 x_i}{\partial \bar{\xi}\partial \bar{\eta}} &= \frac{\partial^2 x_i}{\partial \xi \partial \eta}\frac{\partial \xi}{\partial \bar{\xi}}\frac{\partial \eta}{\partial \bar{\eta}} = \frac{\partial^2 x_i}{\partial \xi \partial \eta}\bar{J}_\xi \bar{J}_\eta
\end{aligned} \tag{55}$$

Now the polar coordinates $\boldsymbol{\rho}(\rho, \theta)$ centred at the source point are introduced in the parent space as in Figure 2, The parent domain is subdivided into four triangles for quadrature naturally. Each triangle is regarded as a degenerated square $[-1, 1]\times[-1, 1]$ with two points joint together. Supposing a point $\boldsymbol{\rho}(\rho, \theta) \in [0, \hat{\rho}(\theta)]\times[\theta_1, \theta_2]$ in the triangle, a linear mapping between the polar coordinates and the square coordinates system $\tilde{\boldsymbol{\xi}}(\tilde{\xi}, \tilde{\eta})$ is performed as:

$$\begin{aligned}
\rho &= \frac{1}{2}(\tilde{\eta} + 1)\hat{\rho}(\theta), \\
\theta &= \frac{1}{2}(\theta_2 - \theta_1)\tilde{\xi} + \frac{1}{2}(\theta_2 + \theta_1).
\end{aligned} \tag{56}$$

And the Jacobian transformation for this would be:

$$\begin{aligned}
\tilde{J}_\rho &= \frac{\partial \rho}{\partial \tilde{\eta}} = \frac{1}{2}\hat{\rho}(\theta), \\
\tilde{J}_\theta &= \frac{\partial \theta}{\partial \tilde{\xi}} = \frac{1}{2}(\theta_2 - \theta_1), \\
\tilde{J}(\boldsymbol{\rho}) &= \tilde{J}_\rho \tilde{J}_\theta.
\end{aligned} \tag{57}$$

Equation (54) becomes:

$$\begin{aligned}
x_i - s_i &= \rho\Big[\frac{\partial x_i}{\partial \bar{\xi}}\Big|_{\bar{\boldsymbol{\xi}}=\bar{\boldsymbol{\xi}}_s}\cos\theta + \frac{\partial x_i}{\partial \bar{\eta}}\Big|_{\bar{\boldsymbol{\xi}}=\bar{\boldsymbol{\xi}}_s}\sin\theta\Big] \\
&\quad + \rho^2\Big[\frac{\partial^2 x_i}{\partial \bar{\xi}^2}\Big|_{\bar{\boldsymbol{\xi}}=\bar{\boldsymbol{\xi}}_s}\frac{\cos^2\theta}{2} + \frac{\partial^2 x_i}{\partial \bar{\xi}\partial \bar{\eta}}\Big|_{\bar{\boldsymbol{\xi}}=\bar{\boldsymbol{\xi}}_s}\cos\theta\sin\theta + \frac{\partial^2 x_i}{\partial \bar{\eta}^2}\Big|_{\bar{\boldsymbol{\xi}}=\bar{\boldsymbol{\xi}}_s}\frac{\sin^2\theta}{2}\Big] + O(\rho^3) \\
&:= \rho A_i(\theta) + \rho^2 B_i(\theta) + O(\rho^3).
\end{aligned} \tag{58}$$

And we define:

$$\begin{aligned} A &:= \left(\sum_{k=1}^{3} [A_k(\theta)]^2 \right)^{\frac{1}{2}}, \\ C &:= \sum_{k=1}^{3} A_k(\theta) B_k(\theta). \end{aligned} \tag{59}$$

The derivatives of $r = |\mathbf{x} - \mathbf{s}|$ are:

$$\begin{aligned} r_{,i} = \frac{x_i - s_i}{r} &= \frac{A_i}{A} + \left(\frac{B_i}{A} - A_i \frac{C}{A^3} \right) \rho + O(\rho^2) \\ &:= d_{i0} + d_{i1}\rho + O(\rho^2). \end{aligned} \tag{60}$$

The term $1/r^3$ is:

$$\begin{aligned} \frac{1}{r^3} &= \frac{1}{A^3\rho^3} - \frac{3C}{A^5\rho^2} + O(\frac{1}{\rho}) \\ &:= \frac{S_{-2}}{\rho^3} + \frac{S_{-1}}{\rho^2} + O(\frac{1}{\rho}). \end{aligned} \tag{61}$$

The NURBS basis function is also expanded as:

$$\begin{aligned} N_a(\boldsymbol{\xi}) &= N_a(\boldsymbol{\xi}_s) + \rho \Big[\frac{\partial N_a}{\partial \xi}\Big|_{\bar{\boldsymbol{\xi}}=\bar{\boldsymbol{\xi}}_s} \bar{J}_\xi \cos\theta + \frac{\partial N_a}{\partial \eta}\Big|_{\bar{\boldsymbol{\xi}}=\bar{\boldsymbol{\xi}}_s} \bar{J}_\eta \sin\theta \Big] + O(\rho^2) \\ &:= N_{a0} + N_{a1}(\theta)\rho + O(\rho^2). \end{aligned} \tag{62}$$

For the surface point $\boldsymbol{\xi}(\xi, \eta)$ in the knot interval $[\xi_1, \xi_2] \times [\eta_1, \eta_2]$, we define two tangential vectors along the ξ and η directions respectively as:

$$\begin{aligned} \mathbf{m}_1 &= \Big[\frac{\partial x}{\partial \xi}, \frac{\partial y}{\partial \xi}, \frac{\partial z}{\partial \xi} \Big], \\ \mathbf{m}_2 &= \Big[\frac{\partial x}{\partial \eta}, \frac{\partial y}{\partial \eta}, \frac{\partial z}{\partial \eta} \Big]. \end{aligned} \tag{63}$$

And we can get the normal vectors through:

$$\bar{\mathbf{n}} = \mathbf{m}_1 \times \mathbf{m}_2 = \Big[\frac{\partial y}{\partial \xi}\frac{\partial z}{\partial \eta} - \frac{\partial z}{\partial \xi}\frac{\partial y}{\partial \eta}, \frac{\partial z}{\partial \xi}\frac{\partial x}{\partial \eta} - \frac{\partial x}{\partial \xi}\frac{\partial z}{\partial \eta}, \frac{\partial x}{\partial \xi}\frac{\partial y}{\partial \eta} - \frac{\partial y}{\partial \xi}\frac{\partial x}{\partial \eta} \Big]. \tag{64}$$

The Jacobian for transformation from parametric space to physical space is the length of the

normal vector $\bar{\mathbf{n}}$:

$$\begin{aligned} J(\boldsymbol{\xi}) &= \Big[\Big(\frac{\partial y}{\partial \xi}\frac{\partial z}{\partial \eta} - \frac{\partial z}{\partial \xi}\frac{\partial y}{\partial \eta}\Big)^2 + \Big(\frac{\partial z}{\partial \xi}\frac{\partial x}{\partial \eta} - \frac{\partial x}{\partial \xi}\frac{\partial z}{\partial \eta}\Big)^2 + \Big(\frac{\partial x}{\partial \xi}\frac{\partial y}{\partial \eta} - \frac{\partial y}{\partial \xi}\frac{\partial x}{\partial \eta}\Big)^2\Big]^{1/2} \\ &:= \Big[\sum_{k=1}^{3} J_k^2(\boldsymbol{\xi})\Big]^{1/2} \end{aligned} \tag{65}$$

The unit normal vector $\mathbf{n}$ could be expressed as:

$$\mathbf{n}(\boldsymbol{\xi}) = \frac{\bar{\mathbf{n}}}{J(\boldsymbol{\xi})}. \tag{66}$$

The component $J_i(\boldsymbol{\xi})$ can be expanded at the source point. For instance:

$$\begin{aligned} J_1(\boldsymbol{\xi}) &= J_1(\boldsymbol{\xi}_s) + \rho\Big[\frac{\partial J_1}{\partial \xi}\Big|_{\bar{\boldsymbol{\xi}}=\bar{\boldsymbol{\xi}}_s}\bar{J}_\xi \cos\theta + \frac{\partial J_1}{\partial \eta}\Big|_{\bar{\boldsymbol{\xi}}=\bar{\boldsymbol{\xi}}_s}\bar{J}_\eta \sin\theta\Big] + O(\rho^2) \\ &:= J_{10} + J_{11}(\theta)\rho + O(\rho^2), \\ \frac{\partial J_1}{\partial \xi} &= \frac{\partial}{\partial \xi}\Big(\frac{\partial y}{\partial \xi}\frac{\partial z}{\partial \eta} - \frac{\partial z}{\partial \xi}\frac{\partial y}{\partial \eta}\Big). \end{aligned} \tag{67}$$

So we can obtain $J_i(\boldsymbol{\xi})$ as:

$$J_i(\boldsymbol{\xi}) = J_{i0} + J_{i1}(\theta)\rho + O(\rho^2). \tag{68}$$

Combining with Equation (66), we arrive at:

$$n_i(\boldsymbol{\xi}) = \frac{1}{J(\boldsymbol{\xi})}[J_{i0} + J_{i1}(\theta)\rho + O(\rho^2)]. \tag{69}$$

Now, all the terms are prepared for the expansion of the integrand. Let's take a simple example:

$$I = \oint_S \frac{r_{,i} n_i(\boldsymbol{\xi}) N_a(\boldsymbol{\xi})}{r^3} \mathrm{d}S. \tag{70}$$

After discretization,

$$I = \int_0^{2\pi}\int_0^{\hat{\rho}(\theta)} \frac{r_{,i} n_i N_a}{r^3} J(\boldsymbol{\xi})\bar{J}(\boldsymbol{\xi})\rho \mathrm{d}\rho \mathrm{d}\theta, \tag{71}$$

where $\bar{J}(\boldsymbol{\xi})$ is from parent to parametric space defined in Equation (53), $J(\boldsymbol{\xi})$ from parametric to physical space defined in Equation (65). $\hat{\rho}(\theta)$ is the upper bound of ρ and can be seen in Figure 2.

And substitute Equations (60)(61)(69)(62) into the discretization:

$$
\begin{aligned}
I &= \int_0^{2\pi}\int_0^{\hat{\rho}(\theta)} \Big[d_{i0}+d_{i1}\rho+O(\rho^2)\Big]\frac{1}{J(\boldsymbol{\xi})}\Big[J_{i0}+J_{i1}\rho+O(\rho^2)\Big]\Big[N_{a0}+N_{a1}\rho+O(\rho^2)\Big] \\
&\qquad \Big[\frac{S_{-2}}{\rho^3}+\frac{S_{-1}}{\rho^2}+O(\frac{1}{\rho})\Big]J(\boldsymbol{\xi})\bar{J}(\boldsymbol{\xi})\rho\mathrm{d}\rho\mathrm{d}\theta \\
&= \int_0^{2\pi}\int_0^{\hat{\rho}(\theta)} \Big[d_{i0}J_{i0}N_{a0}+(d_{i1}J_{i0}N_{a0}+d_{i0}J_{i1}N_{a0}+d_{i0}J_{i0}N_{a1})\rho+O(\rho^2)\Big] \\
&\qquad \Big[\frac{S_{-2}}{\rho^2}+\frac{S_{-1}}{\rho}+O(1)\Big]\frac{1}{\rho J(\boldsymbol{\xi})}J(\boldsymbol{\xi})\bar{J}(\boldsymbol{\xi})\rho\mathrm{d}\rho\mathrm{d}\theta \\
&= \int_0^{2\pi}\int_0^{\hat{\rho}(\theta)} \Big(\frac{I_{-2}}{\rho^2}+\frac{I_{-1}}{\rho}+O(1)\Big)\bar{J}(\boldsymbol{\xi})\mathrm{d}\rho\mathrm{d}\theta,
\end{aligned}
\tag{72}
$$

where I_{-2}, I_{-1} are only functions of θ:

$$
\begin{aligned}
I_{-2} &= S_{-2}d_{i0}J_{i0}N_{a0}, \\
I_{-1} &= S_{-1}d_{i0}J_{i0}N_{a0}+S_{-2}(d_{i1}J_{i0}N_{a0}+d_{i0}J_{i1}N_{a0}+d_{i0}J_{i0}N_{a1}).
\end{aligned}
\tag{73}
$$

Subtracting the explicit singular part in the original integrand in Equation (71), the regular integral will be obtained:

$$
I_{\mathrm{reg}} = \int_0^{2\pi}\int_0^{\hat{\rho}(\theta)} \Big[\frac{r_{,i}n_iN_a}{r^3}J(\boldsymbol{\xi})\rho-\frac{I_{-2}}{\rho^2}-\frac{I_{-1}}{\rho}\Big]\bar{J}(\boldsymbol{\xi})\mathrm{d}\rho\mathrm{d}\theta, \tag{74}
$$

This double integral can be evaluated using normal Gaussian rule. And the explicit part then will be added back and treated in a semi-analytical way. For the source point located in the singular element, a small circle is created to exclude the source point radius ε in physical space. When mapping the circle into the intrinsic polar coordinate, the circle will be distorted generally. The polar coordinate ρ is represented with respect to ε as:

$$
\rho := \alpha(\varepsilon,\theta) = \varepsilon\beta(\theta)+\varepsilon^2\gamma(\theta)+O(\varepsilon^3). \tag{75}
$$

To evaluate the coefficients β and γ, the radius of the circle is given as the Taylor expansion in intrinsic polar coordinates as:

$$
\varepsilon = \rho A(\theta)+\rho^2\frac{C(\theta)}{A(\theta)}+O(\rho^3). \tag{76}
$$

The reversion of this series is:

$$\rho = \alpha(\varepsilon, \theta) = \varepsilon \frac{1}{A} - \varepsilon^2 \frac{C}{A^4} + O(\varepsilon^3). \tag{77}$$

Thus we get:

$$\begin{aligned} \beta &= \frac{1}{A}, \\ \gamma &= -\frac{C}{A^4}, \end{aligned} \tag{78}$$

which are only functions of θ. Then let's first look at the explicit strong singular part given in the limit form as:

$$\begin{aligned} &\lim_{\varepsilon \to 0} \int_0^{2\pi} \int_{\alpha(\varepsilon,\theta)}^{\hat{\rho}(\theta)} \frac{I_{-1}(\theta)}{\rho} \bar{J}(\boldsymbol{\xi}) \mathrm{d}\rho \mathrm{d}\theta \\ &= \lim_{\varepsilon \to 0} \int_0^{2\pi} \int_{\alpha(\varepsilon,\theta)}^{\hat{\rho}(\theta)} \frac{I_{-1}(\theta)}{\rho} \bar{J}(\boldsymbol{\xi}) \tilde{J}(\boldsymbol{\rho}) \mathrm{d}\tilde{\eta} \mathrm{d}\tilde{\xi} \\ &= \lim_{\varepsilon \to 0} \int_0^{2\pi} I_{-1}(\theta) \bar{J}(\boldsymbol{\xi}) \tilde{J}_\theta \Big[\int_{\alpha(\varepsilon,\theta)}^{\hat{\rho}(\theta)} \frac{1}{\rho} \tilde{J}_\rho \mathrm{d}\tilde{\eta} \Big] \mathrm{d}\bar{\xi} \\ &= \lim_{\varepsilon \to 0} \int_0^{2\pi} I_{-1}(\theta) \bar{J}(\boldsymbol{\xi}) \tilde{J}_\theta \Big[\int_{\alpha(\varepsilon,\theta)}^{\hat{\rho}(\theta)} \frac{1}{\rho} \mathrm{d}\rho \Big] \mathrm{d}\tilde{\xi} \\ &= \lim_{\varepsilon \to 0} \int_0^{2\pi} I_{-1}(\theta) \bar{J}(\boldsymbol{\xi}) \tilde{J}_\theta [\ln\hat{\rho}(\theta) - \ln\alpha(\varepsilon, \theta)] \mathrm{d}\tilde{\xi} \\ &= \int_0^{2\pi} I_{-1}(\theta) \bar{J}(\boldsymbol{\xi}) \ln\hat{\rho}(\theta) \tilde{J}_\theta \mathrm{d}\tilde{\xi} - \lim_{\varepsilon \to 0} \int_0^{2\pi} I_{-1}(\theta) \bar{J}(\boldsymbol{\xi}) \ln\alpha(\varepsilon, \theta) \tilde{J}_\theta \mathrm{d}\tilde{\xi} \\ &= \int_0^{2\pi} I_{-1}(\theta) \bar{J}(\boldsymbol{\xi}) \ln\hat{\rho}(\theta) \tilde{J}_\theta \mathrm{d}\tilde{\xi} - \lim_{\varepsilon \to 0} \int_0^{2\pi} I_{-1}(\theta) \bar{J}(\boldsymbol{\xi}) \ln\varepsilon\beta(\theta) \tilde{J}_\theta \mathrm{d}\tilde{\xi} \\ &= \int_0^{2\pi} I_{-1}(\theta) \bar{J}(\boldsymbol{\xi}) \ln\frac{\hat{\rho}(\theta)}{\beta(\theta)} \tilde{J}_\theta \mathrm{d}\tilde{\xi} - \bar{J}(\boldsymbol{\xi}) \ln\varepsilon \lim_{\varepsilon \to 0} \int_0^{2\pi} I_{-1}(\theta) \mathrm{d}\theta \\ &= \int_0^{2\pi} I_{-1}(\theta) \bar{J}(\boldsymbol{\xi}) \ln\frac{\hat{\rho}(\theta)}{\beta(\theta)} \tilde{J}_\theta \mathrm{d}\tilde{\xi}, \end{aligned} \tag{79}$$

where $\tilde{J}(\boldsymbol{\rho})$ is from polar to square coordinates defined in Equation (57). Note that the last term is canceled since:

$$\int_0^{2\pi} I_{-1}(\theta) \mathrm{d}\theta = 0. \tag{80}$$

After integrating the singular term with respect to ρ analytically and with the use of Equations (75)(80), the explicit strong singular integrand is transferred as a regular one-dimensional integral and normal Gaussian rule then can be applied. Similar treatment applies to the explicit

hyper-singular term. The full evaluation for Equation (71) is obtained:

$$I = I_{\text{reg}} + \int_0^{2\pi} I_{-1}(\theta)\bar{J}(\boldsymbol{\xi})\ln\frac{\hat{\rho}(\theta)}{\beta(\theta)}\tilde{J}_\theta \mathrm{d}\tilde{\xi} - \int_0^{2\pi} I_{-2}(\theta)\bar{J}(\boldsymbol{\xi})\Big[\frac{\gamma(\theta)}{\beta^2(\theta)} + \frac{1}{\hat{\rho}(\theta)}\Big]\tilde{J}_\theta \mathrm{d}\tilde{\xi} \tag{81}$$

B Auxiliary displacement and stress fields in M integral

The auxiliary stress field $\sigma_{ij}^{(2)}$ and displacement field $u_j^{(2)}$ are given as:

$$\begin{aligned}
\sigma_{xx} &= \frac{K_I^{(2)}}{\sqrt{2\pi r}}\cos\frac{\theta}{2}\Big(1 - \sin\frac{\theta}{2}\sin\frac{3\theta}{2}\Big) - \frac{K_{II}^{(2)}}{\sqrt{2\pi r}}\sin\frac{\theta}{2}\Big(2 + \cos\frac{\theta}{2}\cos\frac{3\theta}{2}\Big)\\
\sigma_{yy} &= \frac{K_I^{(2)}}{\sqrt{2\pi r}}\cos\frac{\theta}{2}\Big(1 + \sin\frac{\theta}{2}\sin\frac{3\theta}{2}\Big) + \frac{K_{II}^{(2)}}{\sqrt{2\pi r}}\sin\frac{\theta}{2}\cos\frac{\theta}{2}\cos\frac{3\theta}{2},\\
\tau_{xy} &= \frac{K_I^{(2)}}{\sqrt{2\pi r}}\sin\frac{\theta}{2}\cos\frac{\theta}{2}\cos\frac{3\theta}{2} + \frac{K_{II}^{(2)}}{\sqrt{2\pi r}}\cos\frac{\theta}{2}\Big(1 - \sin\frac{\theta}{2}\sin\frac{3\theta}{2}\Big),\\
\tau_{yz} &= \frac{K_{III}^{(2)}}{\sqrt{2\pi r}}\cos\frac{\theta}{2},\\
\tau_{zx} &= -\frac{K_{III}^{(2)}}{\sqrt{2\pi r}}\sin\frac{\theta}{2},\\
\tau_{zz} &= \nu(\sigma_{xx} + \sigma_{yy}),\\
u_x &= \frac{K_I}{2\mu}\sqrt{\frac{r}{2\pi}}\cos\frac{\theta}{2}\left(\kappa - 1 + 2\sin^2\frac{\theta}{2}\right)\\
&\quad + \frac{(1+\nu)K_{II}}{E}\sqrt{\frac{r}{2\pi}}\sin\frac{\theta}{2}\left(\kappa + 1 + 2\cos^2\frac{\theta}{2}\right),\\
u_y &= \frac{K_I}{2\mu}\sqrt{\frac{r}{2\pi}}\sin\frac{\theta}{2}\left(\kappa + 1 - 2\cos^2\frac{\theta}{2}\right)\\
&\quad + \frac{(1+\nu)K_{II}}{E}\sqrt{\frac{r}{2\pi}}\cos\frac{\theta}{2}\left(1 - \kappa + 2\sin^2\frac{\theta}{2}\right),\\
u_z &= \frac{2K_{III}}{\mu}\sqrt{\frac{r}{2\pi}}\sin\frac{\theta}{2}.
\end{aligned} \tag{82}$$

where (r, θ) are the crack tip polar coordinates and $\mu = \frac{E}{2(1+\nu)}$, $\kappa = 3 - 4\nu$.

The auxiliary strain field can be obtained by differentiating u_j with respect to the physical coordinate.

References

[1] L F Martha, P A Wawrzynek, and A R Ingraffea. Arbitrary crack representation using solid modeling. *Engineering with Computers*, 9(2):63–82, 1993.

[2] V Chiaruttini, V Riolo, and F Feyel. Advanced remeshing techniques for complex 3D crack propagation. In *ICF13*, 2013.

[3] A R Khoei, M Eghbalian, H Moslemi, and H Azadi. Crack growth modeling via 3D automatic adaptive mesh refinement based on modified-SPR technique. *Applied Mathematical Modelling*, 37(1):357–383, 2013.

[4] M Schöllmann, M Fulland, and H.A Richard. Development of a new software for adaptive crack growth simulations in 3D structures. *Engineering Fracture Mechanics*, 70(2):249–268, January 2003.

[5] A R Maligno, S Rajaratnam, S B Leen, and E J Williams. A three-dimensional (3D) numerical study of fatigue crack growth using remeshing techniques. *Engineering Fracture Mechanics*, 77(1):94–111, 2010.

[6] R Branco, F V Antunes, and J D Costa. A review on 3D-FE adaptive remeshing techniques for crack growth modelling. *Engineering Fracture Mechanics*, 141:170–195, June 2015.

[7] N Moës, J Dolbow, and T Belytschko. A finite element method for crack growth without remeshing. *International Journal for Numerical Methods in Engineering*, 46(1):131–150, 1999.

[8] N Sukumar, N Moës, B Moran, and T Belytschko. Extended finite element method for three-dimensional crack modelling. *International Journal for Numerical Methods in Engineering*, 48(11):1549–1570, 2000.

[9] N Sukumar, D L Chopp, E Béchet, and N Moës. Three-dimensional non-planar crack growth by a coupled extended finite element and fast marching method. *International Journal for Numerical Methods in Engineering*, 76(5):727–748, 2008.

[10] A Gravouil, N Moës, and T Belytschko. Non-planar 3D crack growth by the extended finite element and level sets-Part II: Level set update. *International Journal for Numerical Methods in Engineering*, 53(11):2569–2586, 2002.

[11] N Moës, A Gravouil, and T Belytschko. Non-planar 3D crack growth by the extended finite element and level sets-Part I: Mechanical model. *International Journal for Numerical Methods in Engineering*, 53(11):2549–2568, 2002.

[12] K Agathos, E Chatzi, S P A Bordas, and D Talaslidis. A well-conditioned and optimally convergent XFEM for 3D linear elastic fracture. *International Journal for Numerical Methods in Engineering*, pages n/a—-n/a, 2015.

[13] S Bordas and B Moran. Enriched finite elements and level sets for damage tolerance assessment of complex structures. *Engineering Fracture Mechanics*, 73(9):1176–1201, 2006.

[14] S P A Bordas and M Duflot. Derivative recovery and a posteriori error estimate for extended finite elements. *Computer Methods in Applied Mechanics and Engineering*, 196(35-36):3381–3399, 2007.

[15] E Wyart, M Duflot, D Coulon, P Martiny, T Pardoen, J.-F. Remacle, and F Lani. Substructuring FE–XFE approaches applied to three-dimensional crack propagation. *Journal of Computational and Applied Mathematics*, 215(2):626–638, 2008.

[16] P Krysl and T Belytschko. The element free Galerkin method for dynamic propagation of arbitrary 3-D cracks. *International Journal for Numerical Methods in Engineering*, 44(6):767–800, 1999.

[17] G Ventura, J X Xu, and T Belytschko. A vector level set method and new discontinuity approximations for crack growth by EFG. *International Journal for Numerical Methods in Engineering*, 54(6):923–944, 2002.

[18] T Rabczuk, S Bordas, and G Zi. On three-dimensional modelling of crack growth using partition of unity methods. *Computers & Structures*, 88(23-24):1391–1411, December 2010.

[19] S P A Bordas, T Rabczuk, and G Zi. Three-dimensional crack initiation, propagation, branching and junction in non-linear materials by an extended meshfree method without asymptotic enrichment. *Engineering Fracture Mechanics*, 75(5):943–960, 2008.

[20] V P Nguyen, T Rabczuk, S Bordas, and M Duflot. Meshless methods: A review and computer implementation aspects. *Mathematics and Computers in Simulation*, 79(3):763–813, 2008.

[21] H Hong and J Chen. Derivations of Integral Equations of Elasticity. *Journal of Engineering Mechanics*, 114(6):1028–1044, 1988.

[22] J T Chen and H K Hong. Review of dual boundary element methods with emphasis on hypersingular integrals and divergent series. *Appl. Mech. Rev.*, 52(1):17–33, 1999.

[23] A Portela, M H Aliabadi, and D P Rooke. The dual boundary element method: Effective implementation for crack problems. *International Journal for Numerical Methods in Engineering*, 33(6):1269–1287, 1992.

[24] Y Mi and M H Aliabadi. Dual boundary element method for three-dimensional fracture mechanics analysis. *Engineering Analysis with Boundary Elements*, 10(2):161–171, 1992.

[25] A P Cisilino and M H Aliabadi. Dual boundary element assessment of three-dimensional fatigue crack growth. *Engineering Analysis with Boundary Elements*, 28(9):1157–1173, 2004.

[26] A P Cisilino and M H Aliabadi. Three-dimensional boundary element analysis of fatigue crack growth in linear and non-linear fracture problems. *Engineering Fracture Mechanics*, 63(6):713–733, August 1999.

[27] V Leitão, M H Aliabadi, and D P Rooke. The dual boundary element formulation for elastoplastic fracture mechanics. *International Journal for Numerical Methods in Engineering*, 38(2):315–333, 1995.

[28] P Fedelinski, M H Aliabadi, and D P Rooke. The dual boundary element method in dynamic fracture mechanics. *Engineering Analysis with Boundary Elements*, 12(3):203–210, January 1993.

[29] S C Mellings and J M W Baynham. Automatic Fatigue Crack Growth. In *ASME 2009 Pressure Vessels and Piping Conference*, pages 1513–1523. American Society of Mechanical Engineers, 2009.

[30] B J Carter, P A Wawrzynek, and A R Ingraffea. Automated 3-D crack growth simulation. *International journal for numerical methods in engineering*, 47(1-3):229–253, 2000.

[31] S Li, M E Mear, and L Xiao. Symmetric weak-form integral equation method for three-dimensional fracture analysis. *Computer Methods in Applied Mechanics and Engineering*, 151(3–4):435–459, 1998.

[32] A Frangi. Fracture propagation in 3D by the symmetric Galerkin boundary element method. *International Journal of Fracture*, 116(4):313–330, 2002.

[33] A Frangi, G Novati, R Springhetti, and M Rovizzi. 3D fracture analysis by the symmetric Galerkin BEM. *Computational Mechanics*, 28(3-4):220–232, 2002.

[34] G P Nikishkov, J H Park, and S N Atluri. SGBEM-FEM alternating method for analyzing 3D non-planar cracks and their growth in structural components. *Computer Modeling in Engineering & Sciences*, 2(3):401–422, 2001.

[35] A Frangi and G Novati. BEM–FEM coupling for 3D fracture mechanics applications. *Computational Mechanics*, 32(4-6):415–422, 2003.

[36] T J R Hughes, J A Cottrell, and Y Bazilevs. Isogeometric analysis: CAD, finite elements, NURBS, exact geometry and mesh refinement. *Computer Methods in Applied Mechanics and Engineering*, 194(39–41):4135–4195, 2005.

[37] M A Scott, R N Simpson, J A Evans, S Lipton, S P A Bordas, T J R Hughes, and T W Sederberg. Isogeometric boundary element analysis using unstructured T-splines. *Computer Methods in Applied Mechanics and Engineering*, 254(0):197–221, 2013.

[38] R N Simpson, S P A Bordas, J Trevelyan, and T Rabczuk. A two-dimensional Isogeometric Boundary Element Method for elastostatic analysis. *Computer Methods in Applied Mechanics and Engineering*, 209–212(0):87–100, 2012.

[39] R N Simpson, M A Scott, M Taus, D C Thomas, and H Lian. Acoustic isogeometric boundary element analysis. *Computer Methods in Applied Mechanics and Engineering*, page accepted, 2013.

[40] J Gu, J Zhang, and G Li. Isogeometric analysis in BIE for 3-D potential problem. *Engineering Analysis with Boundary Elements*, 36(5):858–865, 2012.

[41] K Li and X Qian. Isogeometric analysis and shape optimization via boundary integral. *Computer-Aided Design*, 43(11):1427–1437, 2011.

[42] C Politis, A I Ginnis, P D Kaklis, K Belibassakis, and C Feurer. An isogeometric BEM for exterior potential-flow problems in the plane. In *2009 SIAM/ACM Joint Conference on Geometric and Physical Modeling*, SPM '09, pages 349–354, New York, NY, USA, 2009. ACM.

[43] A I Ginnis, K V Kostas, C G Politis, P D Kaklis, K A Belibassakis, Th.P. Gerostathis, M.A. Scott, and T.J.R. Hughes. Isogeometric boundary-element analysis for the wave-resistance problem using T-splines. *Computer Methods in Applied Mechanics and Engineering*, 279:425–439, September 2014.

[44] K V Kostas, A I Ginnis, C G Politis, and P D Kaklis. Ship-hull shape optimization with a T-spline based BEM–isogeometric solver. *Computer Methods in Applied Mechanics and Engineering*, 284:611–622, February 2015.

[45] M J Peake, J Trevelyan, and G Coates. Extended isogeometric boundary element method (XIBEM) for two-dimensional Helmholtz problems. *Computer Methods in Applied Mechanics and Engineering*, 259(0):93–102, 2013.

[46] M.J. Peake, J. Trevelyan, and G. Coates. Extended isogeometric boundary element method (XIBEM) for three-dimensional medium-wave acoustic scattering problems. *Computer Methods in Applied Mechanics and Engineering*, 284:762–780, February 2015.

[47] G Beer, B Marussig, J Zechner, C Dunser, and T P Fries. Boundary element analysis with trimmed NURBS and a generalized IGA approach. *Arxiv.org*, 2015.

[48] Y Wang, D J Benson, and A P Nagy. A multi-patch nonsingular isogeometric boundary element method using trimmed elements. *Computational Mechanics*, 56(1):173–191, 2015.

[49] B Marussig, J Zechner, G Beer, and T P Fries. Fast isogeometric boundary element method based on independent field approximation. *Computer Methods in Applied Mechanics and Engineering*, 284:458–488, 2015.

[50] M Feischl, G Gantner, and D Praetorius. Reliable and efficient a posteriori error estimation for adaptive {IGA} boundary element methods for weakly-singular integral equations. *Computer Methods in Applied Mechanics and Engineering*, 290:362–386, 2015.

[51] A Aimi, M Diligenti, M L Sampoli, and A Sestini. Isogemetric analysis and symmetric Galerkin BEM: A 2D numerical study. *Applied Mathematics and Computation*, pages –, 2015.

[52] M Taus, G J Rodin, and T J R Hughes. Isogeometric analysis of boundary integral equations. *ICES report 15-12*, 2015.

[53] E De Luycker, D J Benson, T Belytschko, Y Bazilevs, and M C Hsu. X-FEM in isogeometric analysis for linear fracture mechanics. *International Journal for Numerical Methods in Engineering*, 87(6):541–565, 2011.

[54] S Ghorashi, N Valizadeh, and S Mohammadi. Extended isogeometric analysis for simulation of stationary and propagating cracks. *International Journal for Numerical Methods in Engineering*, 89(9):1069–1101, 2012.

[55] V P Nguyen, C Anitescu, S P A Bordas, and T Rabczuk. Isogeometric analysis: An overview and computer implementation aspects. *Mathematics and Computers in Simulation*, 117:89–116, June 2015.

[56] N. Nguyen-Thanh, N. Valizadeh, M.N. Nguyen, H. Nguyen-Xuan, X. Zhuang, P. Areias, G. Zi, Y. Bazilevs, L. De Lorenzis, and T. Rabczuk. An extended isogeometric thin shell analysis based on Kirchhoff–Love theory. *Computer Methods in Applied Mechanics and Engineering*, 284:265–291, February 2015.

[57] C V Verhoosel, M A Scott, R de Borst, and T J R Hughes. An isogeometric approach to cohesive zone modeling. *International Journal for Numerical Methods in Engineering*, 87(1-5):336–360, 2011.

[58] V P Nguyen, P Kerfriden, and S P A Bordas. Two- and three-dimensional isogeometric cohesive elements for composite delamination analysis. *Composites Part B: Engineering*, 60:193–212, April 2014.

[59] M J Choi and S Cho. Isogeometric shape design sensitivity analysis of stress intensity factors for curved crack problems. *Computer Methods in Applied Mechanics and Engineering*, 279:469–496, September 2014.

[60] A. Tambat and G. Subbarayan. Isogeometric enriched field approximations. *Computer Methods in Applied Mechanics and Engineering*, 245-246:1–21, October 2012.

[61] K. Upreti, T. Song, A. Tambat, and G. Subbarayan. Algebraic distance estimations for enriched isogeometric analysis. *Computer Methods in Applied Mechanics and Engineering*, 280:28–56, October 2014.

[62] J W Jeong, H S Oh, S Kang, and H Kim. Mapping techniques for isogeometric analysis of elliptic boundary value problems containing singularities. *Computer Methods in Applied Mechanics and Engineering*, 254:334–352, February 2013.

[63] H S Oh, H Kim, and J W Jeong. Enriched isogeometric analysis of elliptic boundary value problems in domains with cracks and/or corners. *International Journal for Numerical Methods in Engineering*, 97(3):149–180, January 2014.

[64] S Natarajan, J Wang, C Song, and C Birk. Isogeometric analysis enhanced by the scaled boundary finite element method. *Computer Methods in Applied Mechanics and Engineering*, 283:733–762, January 2015.

[65] M Guiggiani. Formulation and numerical treatment of boundary integral equations with hypersingular kernels. *Singular integrals in boundary element methods*, pages 85–124, 1998.

[66] L Piegl and W Tiller. The NURBS book. *springer*, 1995.

[67] Y Liu and T J Rudolphi. Some identities for fundamental solutions and their applications to weakly-singular boundary element formulations. *Engineering Analysis with Boundary Elements*, 8(6):301–311, 1991.

[68] Y.J. Wang and D.J. Benson. Multi-patch nonsingular isogeometric boundary element analysis in 3D. *Computer Methods in Applied Mechanics and Engineering*, 293:71–91, August 2015.

[69] M Guiggiani, G Krishnasamy, T J Rudolphi, and F J Rizzo. A General Algorithm for the Numerical Solution of Hypersingular Boundary Integral Equations. *Journal of Applied Mechanics*, 59(3):604–614, 1992.

[70] J Rong, L Wen, and J Xiao. Efficiency improvement of the polar coordinate transformation for evaluating BEM singular integrals on curved elements. *Engineering Analysis With Boundary Elements*, 38:83–93, 2014.

[71] S Osher and R Fedkiw. *Level set methods and dynamic implicit surfaces*, volume 153. Springer Science & Business Media, 2006.

[72] N Moës, M Cloirec, P Cartraud, and J F Remacle. A computational approach to handle complex microstructure geometries. *Computer Methods in Applied Mechanics and Engineering*, 192(28-30):3163–3177, July 2003.

[73] T J Barth and J A Sethian. Numerical Schemes for the Hamilton–Jacobi and Level Set Equations on Triangulated Domains. *Journal of Computational Physics*, 145(1):1–40, September 1998.

[74] D L Chopp and N Sukumar. Fatigue crack propagation of multiple coplanar cracks with the coupled extended finite element/fast marching method. *International Journal of Engineering Science*, 41(8):845–869, May 2003.

[75] T P Fries and M Baydoun. Crack propagation with the extended finite element method and a hybrid explicit–implicit crack description. *International Journal for Numerical Methods in Engineering*, 89(12):1527–1558, 2012.

[76] A Paluszny and R W Zimmerman. Numerical simulation of multiple 3D fracture propagation using arbitrary meshes. *Computer Methods in Applied Mechanics and Engineering*, 200(9-12):953–966, February 2011.

[77] J Garzon, P O'Hara, C A Duarte, and W G Buttlar. Improvements of explicit crack surface representation and update within the generalized finite element method with application to three-dimensional crack coalescence. *International Journal for Numerical Methods in Engineering*, 97(4):231–273, 2014.

[78] A Paluszny and R W Zimmerman. Numerical fracture growth modeling using smooth surface geometric deformation. *Engineering Fracture Mechanics*, 108(0):19–36, 2013.

[79] R LaGreca, M Daniel, and A Bac. Local deformation of NURBS curves. *Mathematical methods for curves and surfaces, Tromso 2004*, pages 243–252, 2005.

[80] S K Chan, I S Tuba, and W K Wilson. On the finite element method in linear fracture mechanics. *Engineering Fracture Mechanics*, 2(1):1–17, July 1970.

[81] T K Hellen. On the method of virtual crack extensions. *International Journal for numerical methods in engineering*, 9(1):187–207, 1975.

[82] C G Hwang, P A Wawrzynek, and A R Ingraffea. On the virtual crack extension method for calculating the derivatives of energy release rates for a 3D planar crack of arbitrary shape under mode-I loading. *Engineering Fracture Mechanics*, 68(7):925–947, May 2001.

[83] B R Davis, P A Wawrzynek, and A R Ingraffea. 3-D simulation of arbitrary crack growth using an energy-based formulation – Part I: Planar growth. *Engineering Fracture Mechanics*, 115:204–220, 2014.

[84] B R Davis, P A Wawrzynek, and A R Ingraffea. Simulation of Arbitrary Mixed-Mode Crack Growth Using an Energy-Based Approach. In Jay Carroll and Samantha Daly, editors, *Fracture, Fatigue, Failure, and Damage Evolution, Volume 5*, Conference Proceedings of the Society for Experimental Mechanics Series, pages 1–9. Springer International Publishing, 2015.

[85] D Sutula, S P A Bordas, P Kerfriden, and A Barthelemy. Global Energy Minimization for Multi-crack Growth in Linear Elastic Fracture using the Extended Finite Element Methods. *11th. World Congress on Computational Mechanics (WCCM XI)*, Barcelona, 2014.

[86] R Krueger. Virtual crack closure technique: history, approach, and applications. *Applied Mechanics Reviews*, 57(2):109–143, 2004.

[87] J R Rice. A path independent integral and the approximate analysis of strain concentration by notches and cracks. *Journal of applied mechanics*, 35(2):379–386, 1968.

[88] M Stern, E B Becker, and R S Dunham. A contour integral computation of mixed-mode stress intensity factors. *International Journal of Fracture*, 12(3):359–368, 1976.

[89] J F Yau, S S Wang, and H T Corten. A mixed-mode crack analysis of isotropic solids using conservation laws of elasticity. *Journal of Applied Mechanics*, 47:333–341, 1980.

[90] P H Wen, M H Aliabadi, and D P Rooke. A contour integral for the evaluation of stress intensity factors. *Applied mathematical modelling*, 19(8):450–455, 1995.

[91] I Babuška and A Miller. The post-processing approach in the finite element method. Part 2: The calculation of stress intensity factors. *International Journal for numerical methods in Engineering*, 20(6):1111–1129, 1984.

[92] J P Pereira and C A Duarte. Extraction of stress intensity factors from generalized finite element solutions. *Engineering Analysis with Boundary Elements*, 29(4):397–413, April 2005.

[93] R H Rigby and M H Aliabadi. Mixed-mode J-integral method for analysis of 3D fracture problems using BEM. *Engineering Analysis with Boundary Elements*, 11(3):239–256, 1993.

[94] J H Chang and D J Wu. Stress intensity factor computation along a non-planar curved crack in three dimensions. *International Journal of Solids and Structures*, 44(2):371–386, 2007.

[95] G P Nikishkov and S N Atluri. Calculation of fracture mechanics parameters for an arbitrary three-dimensional crack, by the 'equivalent domain integral' method. *International Journal for Numerical Methods in Engineering*, 24(9):1801–1821, 1987.

[96] K N Shivakumar and I S Raju. An equivalent domain integral method for three-dimensional mixed-mode fracture problems. *Engineering Fracture Mechanics*, 42(6):935–959, 1992.

[97] O Huber, J Nickel, and G Kuhn. On the decomposition of the J-integral for 3D crack problems. *International Journal of Fracture*, 64(4):339–348, 1993.

[98] R H Rigby and M H Aliabadi. Decomposition of the mixed-mode J-integral—revisited. *International Journal of Solids and Structures*, 35(17):2073–2099, 1998.

[99] M Gosz and B Moran. An interaction energy integral method for computation of mixed-mode stress intensity factors along non-planar crack fronts in three dimensions. *Engineering Fracture Mechanics*, 69(3):299–319, 2002.

[100] A P Cisilino and J Ortiz. Boundary element analysis of three-dimensional mixed-mode cracks via the interaction integral. *Computer Methods in Applied Mechanics and Engineering*, 194(9-11):935–956, March 2005.

[101] L A de Lacerda and L C Wrobel. Dual boundary element method for axisymmetric crack analysis. *International Journal of Fracture*, 113(3):267–284, 2002.

[102] F Erdogan and G Sih. On the crackextension in plates under plane loading and transverse shear. *Journal of Basic Engineering*, 85:519–527, 1963.

[103] N Sukumar, D L Chopp, and B Moran. Extended finite element method and fast marching method for three-dimensional fatigue crack propagation. *Engineering Fracture Mechanics*, 70(1):29–48, January 2003.